JOURNAL OF PETROLOGY

Journal of Petrology, 2020, 1–25
doi: 10.1093/petrology/egaa066
Advance Access Publication Date: 15 June 2020
Original Manuscript

OXFORD

High Temperature Reduced Granulite-Facies Nature of Garnetites in the Khabarny Mafic–Ultramafic Massif, Southern Urals: Evidence from Fluid and Mineral Analyses

Ronald J. Bakker [1]*, Evgenii Pushkarev[2] and Anna P. Biryuzova[2]

[1]Department of Applied Geosciences and Geophysics, Chair Resource Mineralogy, Montanuniversity, Leoben 8700, Austria; [2]Institute of Geology and Geochemistry, Ural Branch, Russian Academy of Sciences, Ekaterinburg, Russia

*Corresponding author. Telephone: +43 (0)3842 4026211. Fax: +43 (0)3842 47016. E-mail: bakker@unileoben.ac.at

Received 8 February 2020; Accepted 9 October 2020

ABSTRACT

High-grade metamorphic rocks underlying the intrusive layered dunite–pyroxenite–gabbronorite East-Khabarny Complex (EKC) are integrated in the complex Khabarny mafic–ultramafic Massif in the Sakmara Allochthon zone in the Southern Urals. These rocks are associated with high-temperature shear zones. Garnetites from the upper part of the metamorphic unit close to the contact with EKC gabbronorite are chemically and texturally analysed to estimate their formation conditions and fluid regime. Fluids provide crucial information of formation conditions and evolution of these garnetites during high-grade metamorphism, and are preserved in channel positions within $Si_6O_{18}^{12-}$ rings of cordierite, and in fluid inclusions in quartz and garnet. Minerals and fluid inclusions of the garnetites are studied with X-ray fluorescence spectrometry, electron microprobe analyses, Raman spectroscopy, and microthermometry. The garnetites mainly consist of garnet (up to 80 vol. %), cordierite and quartz. Accessory minerals are rutile, ilmenite, graphite, magnetite and cristobalite. Granulite-facies metamorphic conditions of the garnetites are estimated with the garnet–cordierite–sillimanite–quartz geothermobarometer: temperatures of 740 to 830 °C and pressures of 770–845 MPa. The average garnet composition in end-member concentrations is 48·5 mole % almandine (±3·9), 34·7 mole % pyrope (±3·3), 10·3 mole % spessartine (±1·1), 1·8 mole % grossular (±1·5), and 1·5 mole % andradite (±1·5). The cordierite electron microprobe analyses reveal an average Mg^{2+} fraction of 0·79 ± 0·01 in the octahedral site. Relicts of a strong positive temperature anomaly (up to 1000 °C) are evidenced by the preservation of cristobalite crystals in garnet and the high titanium content of quartz (0·031 ± 0·008 mass % TiO_2) and garnet (0·31 ± 0·16 mole % end-member Schorlomite-Al). The fluid components H_2O, CO_2, N_2 and H_2S are detected in cordierite, which correspond to a relatively oxidized fluid environment that is common in granulites. In contrast, a highly reduced fluid environment is preserved in fluid inclusions in quartz nodules, which are mono-fluid phase at room temperature and composed of CH_4 (>96 mole %) with locally minor amounts of C_2H_6, N_2, H_2S and graphite. The fluid inclusions occur in homogeneous assemblages with a density of 0·349 to 0·367 g·cm^{-3}. The CH_4-rich fluid may represent peak-temperature metamorphic conditions, and is consistent with temperature estimation (~1000 °C) from Ti-in-garnet and Ti-in-quartz geothermometry. Tiny CH_4-rich fluid inclusions (diameter 0·5 to 2 μm) are also detected by careful optical analyses in garnet and at the surface of quartz crystals that are included in garnet grains. Graphite in fluid inclusions precipitated at retrograde metamorphic conditions around 300–310 ± 27 °C. Aragonite was trapped simultaneously with CH_4-rich fluids and is assumed to have crystallized at metastable conditions. The initial granulite facies conditions that led to the formation of a cordierite and garnet mineral assemblage must have occurred in a relative

oxidized environment (QFM-buffered) with H_2O–CO_2-rich fluids. Abundant intrusions or tectonic emplacement of mafic to ultramafic melts from the upper mantle that were internally buffered at a WI-buffered (wüstite–iron) level must have released abundant hot CH_4-rich fluids that flooded and subsequently dominated the system. The origin of the granulite-facies conditions is similar to peak-metamorphic conditions in the Salda complex (Central Urals) and the Ivrea–Verbano zone (Italian Alps) as a result of magmatic underplating that provided an appearance of a positive thermal anomaly, and further joint emplacement (magmatic and metamorphic rocks together) into upper crustal level as a high temperature plastic body (diapir).

Key words: cordierite; fluid inclusions; methane; garnetite; granulite; Khabarny mafic–ultramafic massif; Southern Urals

INTRODUCTION

Granulite is a typical high-grade metamorphic rock in the basement of Precambrian platform and shields (e.g. Harley, 1989; Bohlen, 1991 and references therein). Only few granulites are of Phanerozoic age and have formed in active plate margins (e.g. Windley, 1981). Most granulite complexes are included in later tectonic and magmatic events unrelated to their original formation conditions (e.g. Harley, 1989). Consequently, Paleozoic orogens may incorporate Archean or Proterozoic granulite terranes. The formation of Phanerozoic granulite complexes thought to be related to crustal thinning, with emplacement of mantle peridotite, MOHO uprising, and magmatic underplating which provides the occurrence of positive thermal anomaly at the lower crustal level. Such examples are well known in the Ivrea–Verbano zone in the Italian Alps and in the Pyrenees (e.g. Vielzeuf & Kornprobst, 1984; Zingg *et al.*, 1990; Snoke *et al.*, 1999; Barboza *et al.*, 1999).

Several types of granulites are found in the Urals, for example: (1) the Taratash complex, Archean granulite, exhumed basement of the East European platform (Lennykh *et al.*, 1978; Puchkov, 2000; Sindern *et al.*, 2005; Ronkin *et al.*, 2007); and (2) the Salda complex, Devonian granulite, magmatic underplating (Friberg *et al.*, 2000, 2002). In the present study we have analysed high-grade metamorphic rocks of the Khabarny mafic–ultramafic Massif in the Sakmara Allochthon, Southern Urals (Fig. 1). These rocks consist of two-pyroxene granulite, orthopyroxene–biotite–garnet gneiss, pyroxene–garnet amphibolite, pyroxene–garnet–graphite-bearing quartzite and garnetite. The latter is investigated in detail in this study. Numerous solid and fluid inclusions in the mineral assemblage in addition to absorbed fluid components in cordierite of garnetites are the main object of investigation. They are considered along with compositional properties of minerals as key indicators for understanding the nature and temperature–pressure conditions of upper-amphibolite-facies to granulite-facies metamorphism of the East-Khabarny mafic–ultramafic intrusion and the Khabarny Massif as a whole. Magmatic underplating of mafic–ultramafic intrusions is considered as the main cause of high-grade metamorphism in these garnetites, in a similar scenario as was proposed for granulites in the Salda complex (Urals) and the Ivrea–Verbano zone (Italian Alps).

Fluids play an important role in the formation and evolution of rocks and mineral assemblages during high-grade metamorphism (e.g. Harlov, 2012). Relicts of metamorphic fluids are present in fluid inclusions (e.g. Touret, 2001) in a wide variety of metamorphic minerals, and they may be preserved as absorbed volatiles in cordierite (e.g. Rigby & Droop, 2008, and reference therein). The volatile composition of cordierite can be used to examine high-grade metamorphism preserved in granulites (e.g. Harley *et al.*, 2002). The reliability of fluid inclusions as samples of the original peak metamorphic fluid conditions in high-grade metamorphic rock is queried and scrutinized in a number of studies (e.g. Touret, 2001; Kerkhof *et al.*, 2014) and requires detailed knowledge of textures and mineral assemblages of the investigated rock. The mineral assemblage of the garnetites from the Khabarny granulites includes

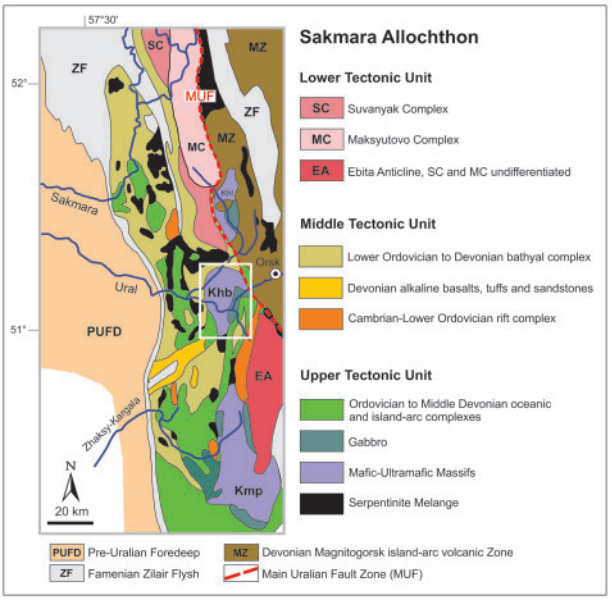

Fig. 1. Simplified tectonic map of the Sakmara Allochthon and surrounding structures, re-drawn after Puchkov (2000, 2002). The white rectangle encloses the Khabarny massif that is illustrated in Fig. 2.

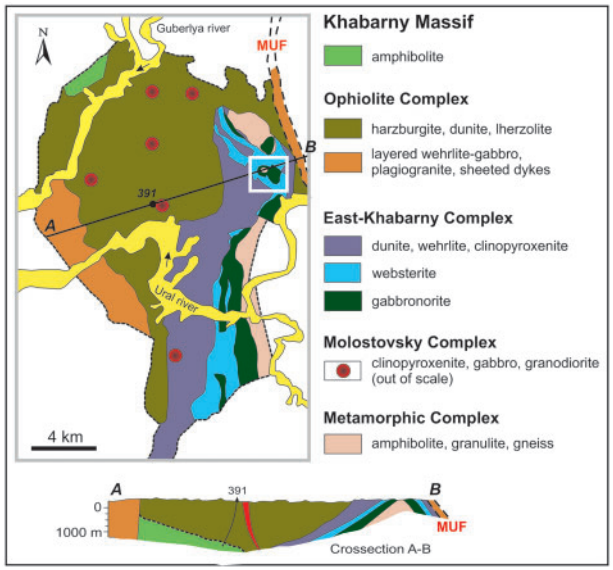

Fig. 2. Simplified geological map of the complex Khabarny mafic–ultramafic massif, redrawn and simplified after Orenburg Regional Geological Survey (1972). The white rectangle encloses the studies area that is illustrated in Fig. 3.

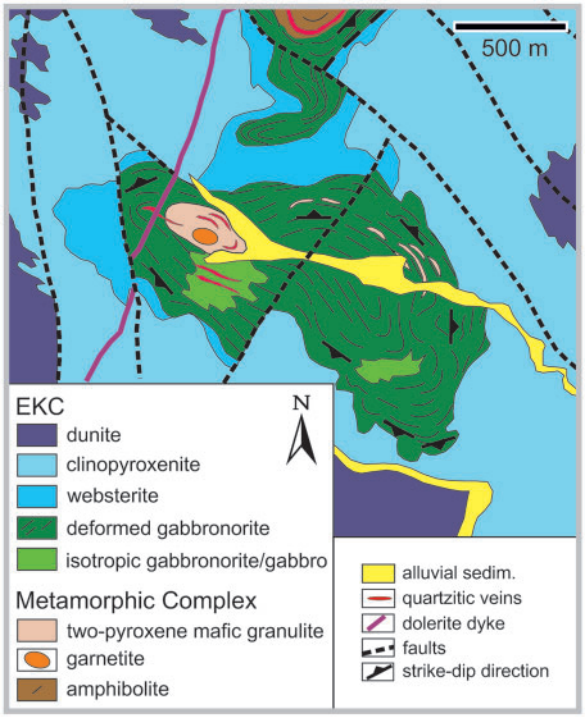

Fig. 3. Simplified geological map of the Kirilovka anticline area, redrawn and modified after Varlakov (1978).

abundant solid inclusions in garnet, cordierite and quartz, in addition to abundant fluid inclusions. The interpretation of fluid inclusion data is directly compared with independent temperature–pressure estimates from garnet–cordierite geothermobarometry and Ti-in-quartz geothermometry in the garnetites. The major mineralogical components are analysed in great detail in the present study, in addition to accessory components and fluid species to characterize the nature of granulite facies metamorphism in the Khabarny allochtone. Furthermore, this study investigates possible post-peak metamorphic modifications of fluid inclusions and cordierite, in addition to investigations of relicts of prograde and retrograde processes.

Sakmara Allochton

The Khabarny mafic–ultramafic Massif belongs to the upper unit of the much larger Sakmara Allochthon in the West Uralian Zone (Puchkov, 2000, 2002, 2013). This zone is described as the Magnitogorsk Accretionary Complex according to Brown *et al.* (2011), and it underwent intensive folding and thrusting, and includes klippe, that contain easterly-derived ophiolites and arc volcanics (Puchkov, 2009, 2013). The Sakmara Allochthon consists of a series of deformed thrust sheets and can be divided in three tectonic units (Fig. 1). The Lower tectonic unit (Uraltau Antiform) contains the Suvanyak Complex (low-grade greenschist facies metamorphic rock) and the Maksyutovo Complex (high-pressure, low-temperature metamorphic rock). The Maksyutovo contains mostly Paleozoic arkose sediments and oceanic volcanics with numerous blocks of gabbro and ultramafic rocks metamorphosed from greenschists up to eclogite facies. The Middle tectonic unit is represented mostly by shales, cherts, limestones and olistostromes of Lower Ordovician to Devonian bathyal rock, in addition to Devonian alkaline basalts and a Lower Ordovician rift complex. The Upper tectonic unit contains mainly different Ordovician to Middle Devonian oceanic and island arc complexes, with mafic–ultramafic complexes (e.g. Khabarny and Kempirsay), that are accompanied by layered wehrlite–pyroxenite–gabbro sequences, sheeted dykes and plagiogranite intrusions (e.g. Savelieva, 2011). A serpentinitic melange comprises numerous blocks of different lithologies and its nature is widespread in the Sakmara Allochton; it is an indicator of the latest tectonic movement, which took place during the closure of the Uralian ocean and collision between East-European paleo-continent and Magnitigorsk island-arc.

Khabarny Mafic–Ultramafic Massif

The Khabarny Massif (Fig. 2) is one of the largest mafic–ultramafic bodies in the Sakmara Allochton. The massif occupies an area of about 400 km^2 and has a plate like shape with a thickness less than 2 km that was established by deep drilling. The Khabarny Massif is located about 30 km to the west of Orsk (Orenburg region, South Urals). It is divided in two unequal parts by the Ural River, which is the national border between Russia and Kazakhstan. The larger northern part belongs to Russia and the smaller southern part belongs to Kazakhstan. The eastern flank of the massif juxtaposes with the Main Uralian Fault-zone that is considered as the root zone for most ophiolite massifs in the Sakmara Allochton (Puchkov, 2000). The Khabarny Massif

comprises several magmatic and metamorphic complexes of different origin and age (Varlakov, 1978; Balykin *et al.*, 1991; Fershtater & Bea, 1996).

The central core is an ophiolite peridotite, mostly highly depleted harzburgite with minor amounts of lherzolite and dunite. The maximum thickness of this ultramafic sequence approaches 1·2–1·5 km (Fig. 2). The underlying rock in the northwestern part are graphite–mica–quartz schists, mafic green-schists and amphibolite, probably of Ordovician and Silurian age. In the SW and NE harzburgite is cut by a crustal ophiolite sequence and comagmatic volcanic rocks, with an assumed age of Silurian to Lower Devonian (Belova *et al.*, 2010).

The East-Khabarny overturned stratified dunite–clinopyroxenite–websterite–gabbronorite Complex (EKC) occurs along the eastern and southeastern margins of the central core ophiolite peridotite (Fig. 2). The thickness of EKC is approximately 2–3 km (Balykin *et al.*, 1991; Fershtater & Bea, 1996). To the west, the contact between EKC and peridotites dips at an angle of 30–45° (see cross-section in Fig. 2). The EKC dunites occur in the upper part of the intrusion, wehrlite, clinopyroxenite and websterite are situated deeper in the central part and gabbronorite develops in the marginal bottom part of the layered body along the contact with the metamorphic complex. The transitional zones between different types of ultramafites and gabbros are sharp but not intrusive. Peridotite xenoliths of the core zone are found in EKC gabbronorite, and EKC websterite dikes occur in the peridotite, which illustrates the intrusive relationship between the ophiolite peridotite and the EKC. All rocks of EKC are enriched in alkali metals, Ti, Rb and Sr, and the chondrite-normalized REE patterns have a negative slope (Fershtater *et al.*, 1997). The pyroxenite comprises titanomagnetite mineralization. From the petrological point of view, EKC may be compared with Ural–Alaskan-type intrusions (Balykin *et al.*, 1991; Fershtater & Bea, 1996).

Small concentrically zoned intrusions are represented by several pipe-like bodies (Molostovsky Complex) cutting the ophiolite peridotite of the central core (Fig. 2). Their size is no more than several hundred metres in diameter. They consist of differentiated clinopyroxenite–gabbro–granodiorite series of Lower Devonian age. Due to similarities in compositions and age, these rocks are assumed to be the fluid-rich equivalents of EKC rocks, with which they connect at depth (Balykin *et al.*, 1991; Fershtater & Bea, 1996).

The metamorphic complex (Fig. 2) has a thickness less than 1 km and underlies the EKC gabbronorite dipping to the WSW at an angle of 20–40° (Biryuzova & Pushkarev, 2007; Pushkarev *et al.*, 2007). We distinguish two units: (1) lower unit of strongly foliated epidote-rich amphibolite (600–900 m thickness) and (2) upper unit (100–150 m thickness) corresponding to granulite–amphibolite facies metamorphic conditions, with rocks that occur in lenses, layers and blocks of two-pyroxene granulite, pyroxene–garnet-bearing amphibolite and quartzite (graphite bearing), orthopyroxene–biotite–garnet gneiss, and rare garnetites. The metamorphic age of amphibolite from this unit was determined by Sm–Nd method and correspond to Early Devonian (415 ± 8 Ma; Pushkarev *et al.*, 2007). The amphibole–garnet geothermometer and the amphibole–plagioclase geobarometer reveal pressure-temperature conditions in the amphibolite facies of 650–750 °C and 500–700 MPa (Biryuzova & Pushkarev, 2007). The transition between these units is sharp and marked by a blastomylonite shear zone of 1–2 m thickness. The contact with the EKC gabbronorite is also strongly foliated in a narrow zone of several metres width (blastomylonite). The structural features of contact show that it is a high-temperature shear zone. The primary intrusive relationship of EKC gabbronorite and highly metamorphic rock is illustrated by the presence of quartzite and granulite xenoliths within the gabbronorite.

Local geological settings of studied garnetite

High-grade metamorphic rocks (granulites) of the upper unit in the metamorphic complex crop out in a small tectonic window within the core of the Kirilovka antiform (Fig. 3), and occupy an area of about quarter of square kilometre on a small hill inbetween two branches of the Kirilovka creek. In addition, relatively small granulitic lenses (2 m thickness, 10–15 m length) are found within the strongly deformed gabbronorite of the EKC. These metamorphic rocks of basic and intermediate composition are mostly represented by fine-grained orthopyroxene and two-pyroxene granulites. Garnetites occur in several individual outcrops within the granulites and are situated close to each-other in an area of about 120 x 50 m. The garnetite is locally situated inbetween gabbronorite and granulite and in some cases along the contact between gabbronorite and quartzite lenses. Relicts of two-pyroxene mafic granulites are found within garnetites (Fig. 4), which demonstrates its metasomatic origin. Generally, the rocks are strongly deformed and demonstrate thin lamination, foliation, boudinage and local folding. The foliation in granulites is concordant with foliation in gabbro blastomylonites of the EKC. Locally, thin garnet-rich veinlets crosscut the granulite. Gabbronorite in the contact zone with garnetites locally contains small crystals of garnet. The presence of a fluid phase is considered to play a major role in the formation of these garnet-rich veins and garnet enrichment in gabbronorite at granulite facies metamorphic conditions. Several graphite-bearing quartzitic veins were distinguished among granulites and as lens-shaped xenoliths in gabbronorite of the EKC.

The age of garnetite was determined by Sm–Nd method using whole rock analyses and mineral fractions of garnet and rutile (Pushkarev *et al.*, 2008), corresponding to Upper Silurian (423 ± 6 Ma, MSWD = 1·9, εNdt= -6·5). The negative εNdt may demonstrate the crustal nature of the garnetite protolith. This age is comparable with the age obtained for accompanying garnet amphibolite (415 ± 8 Ma; Pushkarev *et al.*, 2007).

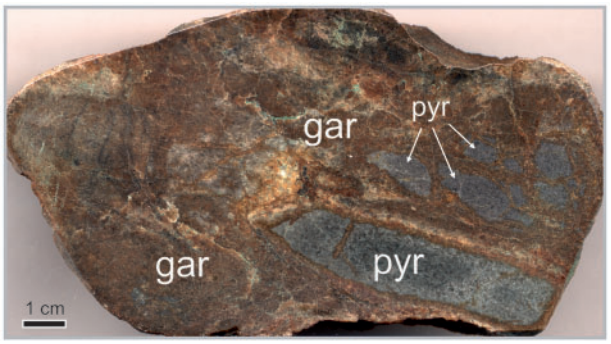

Fig. 4. Rock sample of garnetite (gar) with relicts of two-pyroxene mafic granulites (pyr).

METHODS

Element analyses of rocks and minerals

The rock and mineral compositions are obtained at the Analytical Common Use Centre 'Geoanalyst' of the Institute of Geology and Geochemistry, Ural Division, Russian Academy of Sciences in Ekaterinburg. Bulk rock compositions (except FeO and Na_2O) are determined by X-ray fluorescence spectrometry (XRF) SRM-18. FeO, Na_2O and LOI are determined by routine wet chemical analytical techniques (Kiseleva *et al.*, 2007). Trace element concentrations (including REE) are determined using an Inductively-Coupled-Plasma Mass Spectrometry (ICP-MS) ELAN 9000 (Votyakov *et al.*, 2006). Electron microprobe analyses and backscattered electron (BSE) images of all minerals are obtained using a Cameca SX100 electron microprobe. The Cameca PAP correction software is used for data reduction. An accelerating voltage of 15 kV and beam current of 30 nA is used for all analyses. Typical spot sizes ranged from 3 to 5 μm Na, Mg, Al and Si are measured on TAP crystals; K and Ca, on LPET crystal; Mn, Ti, Fe and Cr, on LIF. The detection limits for the elements analysed are 0·02 mass % (Si, Al, Mg, Ca, Na, K), 0·04 mass % (Ti, Mn), 0·08 mass % (Fe, Cr). The time of pulse acquisition at peaks of analytical lines is two times longer than the time of pulse acquisition at background on both sides from the peak and was 10 s for all elements. Standard deviation (in mass %) varies from 0·24 to 0·30 for Si; from 0·03 to 0·10 for Ti; from 0·03 to 0·25 for Al; from 0·06 to 0·10 for Cr; 0·15 to 0·71 for Fe; from 0·06 to 0·36 for Mn; from 0·08 to 0·18 for Mg; from 0·04 to 0·22 for Ca; from 0·02 to 0·07 for Na; and from 0·01 to 0·03 for K. The electron microprobe standards consist of natural silicates, phosphates and oxide minerals.

Quantitative Ti analyses in quartz are performed with the electron microprobe Superprobe JEOL JXA 8200 in the ESML (Eugen F. Stumpfl Microprobe Laboratory) at the Montanuniversitaet Leoben, Austria. Standardization on rutile and quartz is performed at 20 nA, and a beam current of 200 nA and 15 kV accelerating voltage was used for analyses. The Ti Kα X-rays are counted with the PETH crystal, and Si Kβ X-rays with the TAP crystal to verify that the analysed material is indeed SiO_2. The detection limits of Ti and Si are ~ 7 μg/g and ~ 2300 μg/g, respectively. The standard deviation of Ti analyses is about 2%.

Microthermometry

Fluid inclusions are analysed by microthermometry using a Linkam MDS 600 heating-freezing stage. Calibration was carried out using synthetic fluid inclusions with three invariant temperatures: the melting point of CO_2 at −56·6 °C, the melting of H_2O ice at 0·0 °C, and the critical homogenisation temperature of water at 374·0 °C. The instrument resolution is 0·1 °C, and the standard deviation in each measurement is ±0·2 °C in the range of -150 to +100 °C.

Fluid computer programs

The homogenization conditions of CH_4-rich fluid inclusions are calculated with the software '*LonerSeW*' (software package FLUIDS, http://fluids.unileoben.ac.at, and Bakker, 2003). '*LonerSeW*' uses the definitions of thermodynamic properties of methane according to Setzmann & Wagner (1991). Isochore calculations are restricted to maximally 352 °C and 1000 MPa, but can be extrapolated to higher temperature and pressure conditions. At higher temperature–pressure conditions, the properties of CH_4 can be calculated with the virial equation of state defined by Belonoshko & Saxena (1991) in '*Loner23*' (Bakker, 2003).

Raman spectroscopy

A LabRAM HR Evolution confocal Raman spectrometer (HORIBA, Jobin Yvon GmbH) equipped with an OLYMPUS light microscope is used to record the Raman spectra. The emission line of a HeNe laser (632·817 nm, 17 mW) and an air cooled frequency doubled Nd: YAG laser (532·06 nm, 100 mW) are used for excitation. The remaining power of the Nd: YAG laser at the sample after passing the optics of the Raman spectrometer is about 1–1·5 mW. The single stage spectrometer is an 800 mm focal length Czerny-Turner type spectrograph, equipped with 1800 gr/mm and 600 gr/mm (gratings), an Edge filter, and a multichannel air cooled (-70 °C) CCD detector (1024 x 256 pixels, open electrode front illuminated chip). The spectral resolution is 0·30–0·19 cm^{-1} per pixel at a Raman shift of 100–3500 cm^{-1}, respectively, with a 1800 gr/mm and 633 nm laser. Spatial resolution is downsized to a minimum of 2 μm in the confocal mode with a Olympus 100x objective (plan achromatic, n.a. 0·7). The wavenumbers are calibrated with the Rayleigh scattering (0 cm^{-1}), and a silicon wafer (520·7 cm^{-1}).

Raman spectroscopy has been applied to identify fluids in inclusions as well as solid inclusions in garnet, cordierite and quartz. Cordierite is characterized with Raman spectroscopy to identify molecular fluid components within its crystal structure (e.g. Schreyer, 1985; Kolesov & Geiger, 2000; Kaindl *et al.*, 2006; Rigby & Droop, 2008; Haefecker *et al.*, 2013). The microscope is equipped with a circular rotating stage (vertical rotation

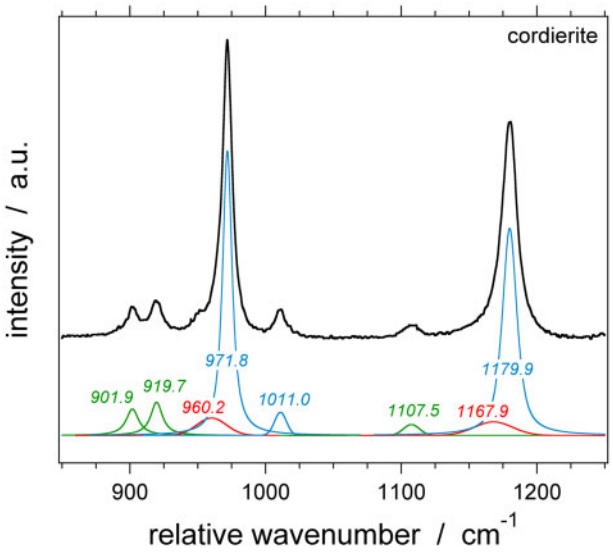

Fig. 5. Best-fit Gaussian-Lorentzian distribution curves of cordierite Raman spectrum. The black curve is the measured spectrum, the blue curves are the main bands. The red curves are the lower wavenumber shoulders of the main curves. The green curves are not taken into account for the orientation estimation.

axis) to orientate cordierite crystal into extinction positions in crossed polarized light settings. The Raman spectra of graphite included in fluid inclusions in quartz, in solid inclusions in garnet, and as intergranular grains between garnet, cordierite and quartz are used to identify its crystallinity and formation temperatures. In general, all accessory mineral phases are identified with Raman spectroscopy.

Raman spectra are analysed with the software PeakFit version 4.12 (2003, SeaSolve Software Inc., USA) to identify best-fit distribution curves to characterize the individual Raman bands, including centre peak position, width (*FWHM*), amplitude and area. All bands are fitted to combined Gaussian and Lorentzian distribution curves, which resulted in the most accurate reproduction of raw spectra. The settings of fitting in the software PeakFit are: automatic fitting using residuals; baseline fitting cubic D2; smoothing level with the Savitzky-Golay algorithm; peak function Gauss + Lorentz sum (area); vary width and vary shape; determination of a_0 (area), a_1 (centre), a_2 (width) and a_3 (shape).

Cordierite Raman analyses

The lattice related Raman bands of cordierite are deconvolved in eight distribution curves in the range of 850–1250 cm^{-1} (Fig. 5). The major bands at 971·8 and 1179·9 cm^{-1} are asymmetric that can be reproduced by adding a small band at lower wavenumbers (960·2 and 1167·9 cm^{-1}). These smaller bands cannot be resolved from the main bands, therefore, the sum of both define the intensity (area) of the main band. The band at 1011 cm^{-1} is relatively small in this specific orientation of the cordierite crystal.

Table 1: Relative intensities (amplitude) of three cordierite Raman bands, normalized to the value at 972 cm^{-1} (100%). Graphically estimated from Fig. 1 in Kolesov & Geiger (2000). These relative numbers can be used as a reference to estimate approximate orientations

Orientation	Raman bands		
	972 ± 1 cm^{-1}	1010 ± 1 cm^{-1}	1180 ± 1 cm^{-1}
XX (aa)	100	6	79
YY (bb)	100	8	20
ZZ (cc)	100	191	9

The orientation of cordierite crystals with reference to the polarization (electric field vector) of the incident laser source of the Raman spectrometer is the essential parameter to interpret the Raman bands of fluid species (Kolesov & Geiger, 2000). The amplitudes of cordierite lattice related Raman bands and bands of absorbed volatiles are strongly dependent on the orientation of the crystal relative to the polarization direction of the laser. The crystallographic orientation of cordierite (orthorhombic crystal system) in thin and thick-sections is difficult to determine with optical microscopy using only one vertical rotation axis. Any two dimensional section through a cordierite crystal has four extinction positions (at 90 °) in the crossed-polarizers mode of an optical microscope, which are not necessary corresponding to the orientation of the crystallographic axes. The most favourable orientation corresponds to the maximum intensity of the CO_2 Raman band at 1382 cm^{-1} in comparison to the cordierite Raman bands at 972 and 1180 cm^{-1}. CO_2 molecules within cordierite channels are preferentially aligned parallel to the *a*-axis (corresponding to the *X* ellipsoid axis of the biaxial indicatrix) (e.g. Johannes & Schreyer, 1981; Armbruster & Bloss, 1982). Therefore, the highest intensity of CO_2 Raman bands is obtained if the polarization plane of the incident laser is parallel to the *a*-axis, also described as the *E//a* orientation (e.g. Aines & Rossman, 1984), the *XX* orientation (e.g. Kolesov & Geiger, 2000) and *aa* orientation (Haefeker *et al.* 2013). H_2O molecules may be orientated with the H-H vector (i.e. perpendicular to the dipole) parallel to the *c*-axis (Type I) or parallel to the *b*-axis (Type II) (e.g. Goldman *et al.*, 1977; Aines & Rossman, 1984; Schreyer, 1985). N_2 is orientated similar to CO_2 molecules within the channels (Armbruster, 1985).

The properties of lattice related Raman bands of cordierite that are measured from crystals in extinction position are used to estimate the approximate crystallographic orientation to obtain ideal conditions to measure the volatile components in cordierite. The relative intensities (amplitude) of the Raman bands at 972 ± 1 cm^{-1}, 1010 ± 1 cm^{-1} and 1180 ± 1 cm^{-1} are indicative for these specific crystallographic orientations (Table 1).

Graphite Raman analyses

The application of Raman spectroscopy to characterize graphite has been described in detail by Beyssac &

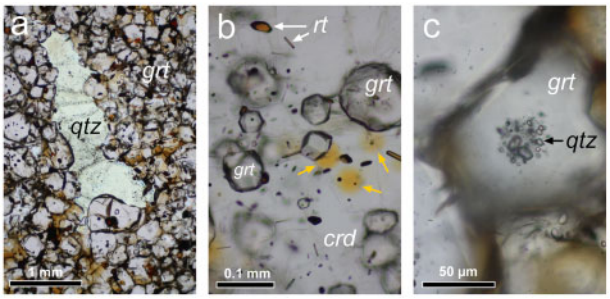

Fig. 6. Photomicrographs of the garnetite, (a) with quartz nodules in a garnet-rich environment, (b) euhedral garnet and rutile crystals in cordierite with yellow radiation damage halos, yellow arrows, and (c) numerous single quartz crystals in the centre of garnet.

Lazzeri (2012, and references therein). Raman spectra contain a true graphite peak (G) and numerous defect peaks (D) that are directly related to the crystal structure, which may vary along different geological environments. The shape of the graphite spectrum can be reproduced according to numerous best-fit distribution curves, and the properties of these curves can be used to determine graphite formation conditions. Lünsdorf *et al.* (2014) and Lünsdorf & Lünsdorf (2016) noticed that the process of this curve-fitting procedure is biased by subjectivity, because many approaches require manual intervention. The determination of the baseline is of major importance to the description of G and D bands, but it is only poorly defined because the broad signal of graphite may cover a range of up to several 100 cm^{-1}. The software *IFORS* (Lünsdorf & Lünsdorf, 2016) is used in the present study to eliminate this subjectivity with an automated fitting procedure including a series of pseudo-Voigt distribution curves. This standardised automatic approach of curve-fitting procedures allow an objective analyses of graphite D and G bands, which can be used as a geothermometer in the range of 160–600 °C. A reference series of carbonaceous material bearing metasediments with well-established metamorphic conditions was provided by G. Rantitsch (Montanuniversity Leoben, Austria). The sum of intensities (amplitude) of the sum-curve at 512 evenly separated points within the selected spectral range 1000–1800 cm^{-1} is normalized to the maximum intensity in the D-band and subsequently normalised to the maximum intensity in the G-band, i.e. the scaled total area method (STA) (Fig. 4, equations 1 and 2 in Lünsdorf *et al.*, 2017). Subsequently, the *STA-RSCM* method (Lünsdorf & Lünsdorf, 2016; Lünsdorf *et al.*, 2017) is used to calculated formation temperatures of graphite.

RESULTS

Petrography and mineralogy of garnetites

We have analysed garnetite samples *Hb1923*, *Hb1924*, *Hb1925*, *Hb1933*, *Hb1966* and *Hb2017* for the present study. Garnetites in the upper unit of the metamorphic complex have a dark-brownish colour and a deformed granoblastic texture. They are mainly composed of fine-grained almandine–pyrope-rich garnets, magnesian-rich cordierite and quartz (Fig. 6). The volume fraction of garnet exceeds 50%, and may approach 80–90 vol. %. The amount of cordierite and quartz approach maximally 20 vol. % and 12 vol. %, respectively. Accessory minerals are rutile, ilmenite, graphite, magnetite and cristobalite. Sillimanite, plagioclase (albite to labradorite), phlogopite, biotite, zircon, monazite, chalcopyrite, pyrite (partly Ni-rich), apatite, aragonite and spinel are present in minor amounts. Clinopyroxene (Mg-number 0·73–0·80) is a rare mineral in garnetites. Rutile is the most widespread accessory mineral. It forms red-brownish transparent equant to elongated crystals (up to 50 µm in length) in groundmass and as inclusions within garnet and other minerals. Graphite forms flakes and plates, but rarely it has cubic and spheroidal shapes. The chemical composition (mass % of oxides and LOI) of the whole-rock garnetite is illustrated in Table 2. The major mineral content observed by optical microscopy (Table 2) illustrates that the relatively high SiO_2 content in sample *Hb1924* is caused by the presence of abundant quartz nodules.

The garnet has a pink to light-red-yellowish colour, and grain sizes varying between 0·05 to 0·8 mm in diameter (Fig. 6a), mostly 0·5 mm. Garnet contains abundant solid inclusions that are located in the centre of single crystals. Small fluid inclusions (sizes up to 0·5 µm in diameter) are identified, mainly by spectroscopic methods. Cordierite occupies the intergranular space between garnets with grain sizes between 10 and 200 µm in diameter. Locally, cordierite grains include completely smaller euhedral garnet crystals (Fig. 6b). Cordierite also contains inclusions of idiomorphic octahedral shaped green spinel (5 to 20 µm diameter). Cordierite is locally marked by yellow radiation halos, caused by µm-sized zircon inclusions (Fig. 6b). The contact between cordierite and garnet does not reveal any reaction textures. Locally, cordierite is altered by pinitization processes into fine-grained muscovite-rich aggregates. Quartz aggregates with a maximum length of a few mm occur in larger irregular elongated nodules between garnet crystals (Fig. 6a). The nodules contain abundant fluid inclusions and locally thin rutile needles. Quartz also occurs in clusters of about 10–20 isolated euhedral crystals (each of 5–20 µm in diameter) in the centre of each garnet grain (Fig. 6c). Cristobalite crystals within these clusters cannot be optically distinguished, but are detected by Raman analyses, often accompany these quartz crystals.

Garnet crystal chemistry

Detailed garnet compositions from the garnetites are revealed in Supplementary Data Electronic Appendix 1; supplementary data are available for downloading at http://www.petrology.oxfordjournals.org. The average garnet composition in end-member concentrations (Fig. 7) according to the method of Locock (2008) is

Table 2: X-ray fluorescence data (whole-rock chemical composition) of garnetites in the Kirilovka anticline. Numbers in mass %. nd, not determined. Approximate volume fractions (%) of mineral phases are indicated in brackets

Sample	Hb1923	Hb1924	Hb1925	Hb1933	Hb1996	Hb2017
SiO_2	34·91	53·58	36·01	34·81	35·72	33·62
TiO_2	1·37	1·38	1·61	1·52	1·42	1·43
Al_2O_3	24·33	14·74	26·04	24·47	24·91	24·53
Fe_2O_3	7·07	2·64	4·52	7·24	5·11	6·07
FeO	19·50	16·80	18·34	19·20	18·75	21·41
MnO	3·93	3·50	3·32	4·07	3·52	4·01
MgO	4·71	3·30	4·20	4·98	5·81	5·41
CaO	1·34	1·66	1·06	1·32	1·03	1·01
Na_2O	0·40	0·60	0·50	0·30	0·40	0·45
K_2O	0·58	0·12	2·56	0·13	0·35	0·76
P_2O_5	0·04	0·23	0·04	0·03	0·30	0·28
LOI	2·45	1·88	2·43	1·80	1·95	1·84
Total	100·63	100·44	100·63	99·87	99·27	100·82
Rb, μg/g	nd	nd	19	nd	2	nd
Sr, μg/g	19	85	23	77	23	86
mineral phases	garnet (60) cordierite (30) rutile (5)	garnet (50) cordierite (30) quartz (10) rutile (3)	garnet (45) cordierite (45) rutile (3)	garnet (65) cordierite (25) sillimanite (3) rutile (3)	garnet (50) cordierite (40) rutile (3)	garnet (70) cordierite (20)

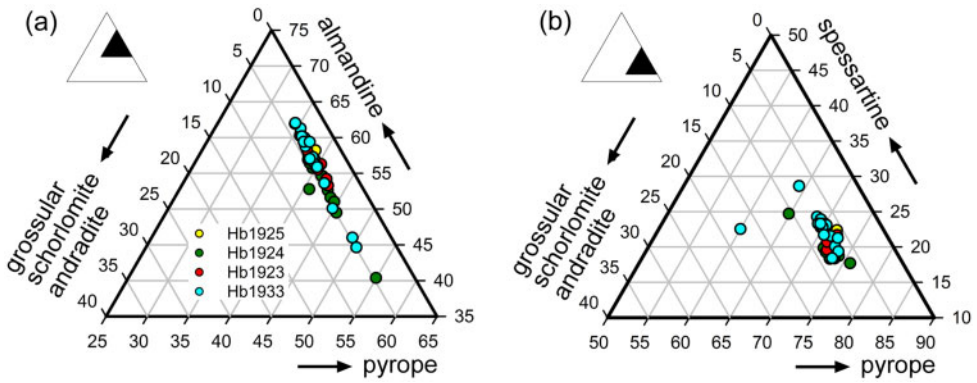

Fig. 7. Garnet analyses of the garnetites in compositional triangular diagrams according to end-member concentrations (see Supplementary Data Electronic Appendix 1).

48·5 mole % almandine (±3·9), 34·7 mole % pyrope (±3·3), 10·3 mole % spessartine (±1·1), 1·8 mole % grossular (±1·5), 1·5 mole % andradite (±1·5). The garnet crystals have homogenous compositions, without significant zoning between core and rim. Slightly regressive and progressive zoning is rarely observed. The variation in Fe^{2+} and Mg^{2+} concentration represented by almandine and pyrope end-members is considerable: 35·05–54·17% almandine, and 29·81– 47·7% pyrope, respectively. The relative mole ratio of Mg^{2+} in the dodecahedral site in garnet compared to the sum of Fe^{2+} and Mg^{2+} is 0·42 ± 0·04. This value is recalculated to 0·37 ± 0·04 compared to the sum of Fe^{2+}, Mg^{2+} and Mn^{2+}. The composition of garnets is consistent with general trends in granulite facies and amphibolite facies rock according to the affinities defined by Suggate & Hall (2018).

Titanium solubility in quartz and garnet

The solubility of Ti in quartz is illustrated in Fig. 8, and corresponding Supplementary Data Electronic Appendix 2. Single isolated quartz crystals that are included in garnet reveal a relatively homogeneous distribution of Ti. Most values are in the range of 0·02–0·04 mass % TiO_2, with an average value of 0·031 (± 0·008) mass % TiO_2 (Fig. 8a). This value corresponds to a mole fraction of 231 (± 60) $\times 10^{-6}$ TiO_2. Quartz in nodules, outside garnet grains have lower Ti values and a larger variation between 0·002–0·044 mass % TiO_2 (Fig. 8b). The garnets reveal a relatively homogeneous Ti solubility, in the range of 0·0052–0·0064 Ti cations per formula based on a 12 oxygen atom normalization (Table 3, Supplementary Data Electronic Appendix 1). This concentration corresponds to 0·31 ± 0·16 mole % of end-member Schorlomite-Al.

Cordierite crystal chemistry

The cordierite electron microprobe analyses are revealed in Supplementary Data Electronic Appendix 3. The average ratio of Mg^{2+} compared to the sum of Fe^{2+}, Mg^{2+} and Mn^{2+} at the octahedral site in the cordierite lattice is 0·79 ± 0·01. The large channel positions

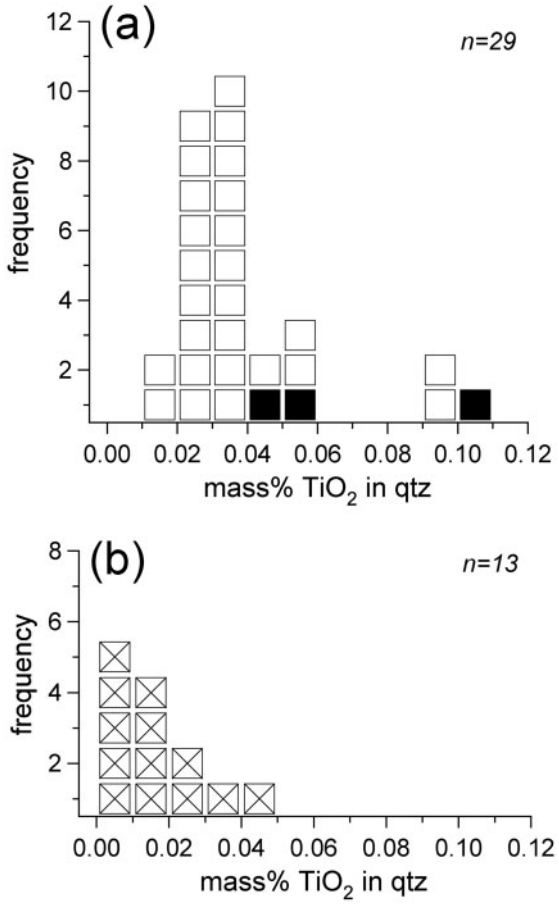

Fig. 8. Histogram of TiO_2 electron microprobe analyses of (a) single quartz crystals in clusters within garnet; and (b) quartz nodules. The black symbols represent exceptional high values in analyses close to rutile grains.

Table 3: The number Ti ions per formula based on a 12-oxygen atom normalization of garnets (see Supplementary Data Electronic Appendix 1). The number of measurements are given in brackets

Sample	Average	Range
Hb1923	0·0064 (6)	0·0029– 0·0139
Hb1924	0·0054 (16)	0·0029– 0·0116
Hb1925	0·0052 (6)	0·0029– 0·0081
Hb1933	0·0058 (21)	0·0006– 0·0164

within the $Si_6O_{18}^{12-}$ rings of cordierite are partly filled with minor amounts of Na^+ ions (0·044 ± 0·019 apfu) and highly variable amounts of Ca^{2+} ions (between 0–0·216 apfu).

The Raman spectra of cordierite are studied in detail to characterize the presence of fluid components within its crystal structure. An example of a CO_2-rich cordierite Raman spectrum orientated in two extinction positions is illustrated in Fig. 9. The properties of best-fit Gaussian-Lorentzian distribution curves of these cordierite Raman bands are given in Tables 4 and 5. The intensity ratios of the Raman bands at approximately

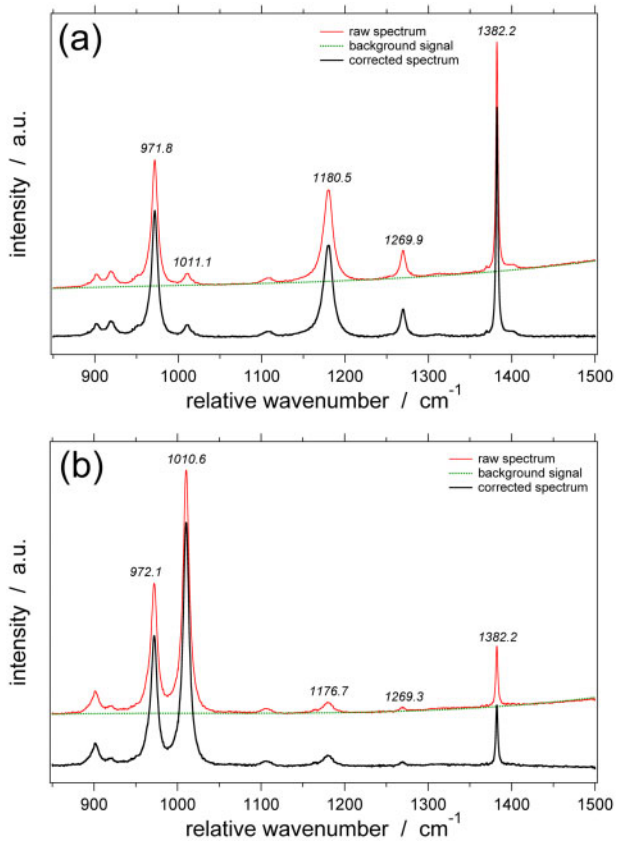

Fig. 9. Raman spectra of cordierite (a) in the XX orientation and (b) ZZ orientation. The Raman bands of CO_2 at 1269.9 and 1382.2 cm^{-1} are better resolved in the XX orientation than the ZZ orientation.

972 cm^{-1}, 1010 cm^{-1} and 1180 cm^{-1} correspond to the orientations *XX* (Fig. 9a, Table 4) and *ZZ* (Fig. 9b, Table 5). The crystallographic axes *a* and *c* of this cordierite crystal are approximately positioned within the two dimensions of the thin sections, and the *b* axis is perpendicular (i.e. vertical) to the microscope table. These orientations reveal the best possible Raman bands (i.e. the highest relative intensity) of the fluid components CO_2, N_2, H_2S and H_2O (Figs 9 and 10).

CO_2 within the cordierite channels reveal a main Raman band at 1382·2 cm^{-1} and a minor band at 1269·9 cm^{-1}, corresponding to the Fermi double (e.g. Garrabos *et al.*, 1989) with a relative amplitude ratio of 8·37 in the XX orientation and 17·64 in the ZZ orientation (Fig. 9, Tables 4 and 5). This ratio is much larger compared to CO_2 in fluid inclusions with an amplitude ratio of approximately 1·9. The peak positions of the Fermi double and the wavenumber distance between these peaks (i.e. 112·3 cm^{-1}) do not correspond to a vapour- and a liquid-like CO_2 fluid, but resembles the characteristics of CO_2 in a clathrate structure (c.f. peak positions at 1276·4 cm^{-1} and 1381·1 cm^{-1}, see Fig. 37 in Bakker, 2016). In detail, the band at 1382·2 cm^{-1} incorporates also the band of the isotope variation $^{13}CO_2$ at 1369·8 cm^{-1}, and a broad band at 1394·9 cm^{-1} that forms a platform at the

Table 4: Best-fit Gaussian-Lorentzian distribution curves of Raman bands of lattice-related vibrations in cordierite, and fluid species within the channels, corresponding to the spectrum illustrated in Fig. 9a (*XX* orientation)

Raman band *(cm^{-1})*	Classification	Area *(a.u.)*	Amplitude *(a.u.)*	Width *(cm^{-1})*	Gauss factor
971·8	SiO_4 (ν_1)	14673·8	1162·5	8·4	0·0883
(960·2)*		(1940·2)	(70·9)	(25·7)	(1·0)
1011	SiO_4 (ν_2)	1052·7	94·4	10·3	0·9373
1179·9	SiO_4 (ν_3)	15483·8	846·1	12·8	0·2034
(1167·9)*		(1954·3)	(55·4)	(33·2)	(1·0)
1269·6	CO_2 (ν_1)	2645·2	261·8	7·3	0·0345
1369·8	$^{13}CO_2$ (ν_1)	50·2	23·0	2·1	1·0
1382·2	CO_2 ($2\nu_2$)	9165·9	2191·0	2·8	0·1304
1394·9	CO_2 (base)	1627·3	38·6	27·9	0·0811
2325·5	N_2 (ν_1)	1362·8	1004·3	1·0	0·2646
2603·2	H_2S (ν_1)				
3598·2	H_2O (ν_1) Class I and II	6853·3	1226·4	3·8	1·0
(3585·4)*	(2144·8)	(55·0)	(25·8)	(1·0)	

*minor shoulder at main peak.

Table 5: Best-fit Gaussian-Lorentzian distribution curves of Raman bands of lattice-related vibrations in cordierite, and fluid species within the channels, corresponding to the spectra illustrated in Fig. 9b (*ZZ* orientation)

Raman band *(cm^{-1})*	Classification	Area *(a.u.)*	Amplitude *(a.u.)*	Width *(cm^{-1})*	Gauss factor
972·1	SiO_4 (ν_1)	11207·5	836·1	8·5	0·0
(964·6)*		(1781·5)	(83·9)	(13·5)	(0·0)
1010·3	SiO_4 (ν_2)	18382·9	1521·2	8·1	0·1150
(1008·0)*		(3064·7)	(134·3)	(21·4)	(1·0)
1180·1	SiO_4 (ν_3)	1182·8	67·6	14·1	0·5591
(1163·8)*		(146·1)	(15·6)	(6·8)	(0·2768)
1269·5	CO_2 (ν_1)	324·4	23·7	8·7	0·0
1382·3	CO_2 ($2\nu_2$)	1859·8	418·0	2·8	0·0036
2325·5	N_2 (ν_1)	569·8	380·7	1·3	0·7483
3598·1	H_2O (ν_1) Class I and II	14250·0	2536·0	3·9	0·1977
(3580·5)*	(2799·7)	(88·5)	(24·8)	(0·4830)	

*minor shoulder at main peak.

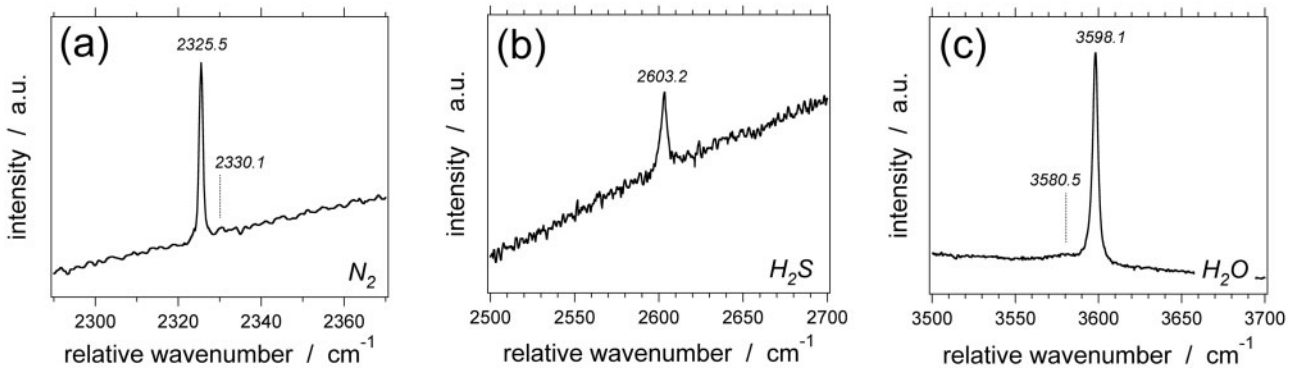

Fig. 10. Raman spectra of cordierite with (a) N_2 in the XX orientation; (b) H_2S in the XX orientation and (c) H_2O in the ZZ orientation.

base of the main band at 1382·2 cm^{-1} (Tables 4 and 5). The intensity (area) of the CO_2 peak is about 5 x as large in the XX position compared to the *ZZ* position.

The Raman bands of N_2 in cordierite channels can be distinguished from atmospheric N_2 (Fig. 10a), with centre positions at 2325·5 cm^{-1} and 2330·1 cm^{-1}, respectively. The intensity (area) of the N_2 peak is about 2·4 x as large in the XX position compared to the *ZZ* position (Tables 4 and 5). H_2S within the cordierite channels reveal a Raman band at 2603·2 cm^{-1} (Fig. 10b). Two types of H_2O vibration modes are visualized in cordierite: a Raman band at 3598·1 cm^{-1} and a relative low shoulder at 3580·5 cm^{-1} (Fig. 10c). The centre position of the latter includes a large uncertainty due to the weakness of the signal. H_2O reveals the highest intensity in the *ZZ* orientation (Tables 4 and 5) in contrast to the orientation

effect for CO_2 and N_2. The intensity of the H_2O peak at 3598·2 cm^{-1} is twice as large as in the XX orientation, whereas the lower peak at 3580–3585 cm^{-1} remains nearly constant in both orientations.

Fluid and solid inclusions in garnet and quartz

Garnet in the garnetites contains abundant solid inclusions (Figs 6c and 11) that are identified with Raman spectroscopy as quartz, cristobalite, ilmenite, rutile, graphite, magnetite, cordierite, phlogopite, plagioclase (variable Na–Ca content, from albite to labradorite) and zircon (Raman spectra are presented in Supplementary Data Electronic Appendix 4). Rutile with euhedral crystals of blocky habit up to 100 μm in length are often partly overgrown by garnet, whereas smaller crystal may be completely enclosed. Ilmenite occurs as equant and rounded crystals (up to 30 μm in diameter) in garnet (Fig. 11a). Equant zircon crystals do not exceed sizes of 2 μm in diameter. Most quartz inclusions in garnet have a perfect crystal shape with clear crystallographic faces, and a variable size of 2–20 μm in diameter (Fig. 11b). Locally, apparent quartz inclusions are identified by Raman spectroscopy as cristobalite (see photomicrograph in Fig. 12; Supplementary Data Electronic Appendix 4), i.e. the high temperature polymorph of quartz. Some quartz inclusions in garnet reveal re-equilibration textures (Fig. 12c and d), with numerous irregular channels and cracks (max. 10 μm length) extending from the quartz surface into the garnet. This texture can be interpreted as a deformation halo around quartz crystals that is originally caused by differential volumetric properties of a quartz polymorph and garnet during temperature–pressure modifications (c.f. Korsakov *et al.*, 2007).

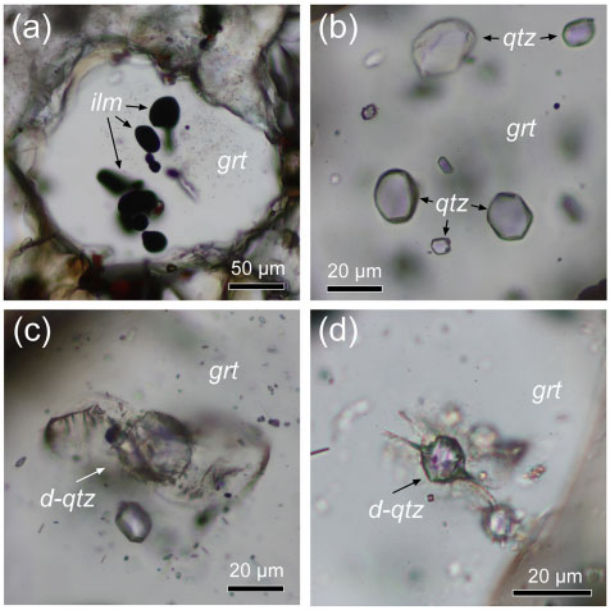

Fig. 11. Photomicrographs of solid inclusions in garnet: (a) rounded ilmenite crystals; (b) euhedral quartz; (c and d) deformation texture around quartz (*d-qtz*).

Multi-component fluid inclusions with entrapped pyrophyllite and siderite crystals, in addition to a fluid mixture of CH_4 (79 ± 4 mole %) and N_2 (21 ± 4 mole %) are rarely observed within the garnet (Fig. 12). These inclusions are smaller than 2 μm in diameter and they are easily overlooked. The phases within these inclusions cannot be optically identified, but their presence is verified with Raman spectroscopy.

Abundant fluid and solid inclusions are observed in quartz crystals within nodules between garnet and cordierite grains (Figs 6a and 13). The fluid inclusions are mono-fluid phase at room temperature. Raman spectroscopy reveals the presence of CH_4 (>96 mole %), and locally minor amounts of C_2H_6, N_2 and H_2S (Fig. 14).

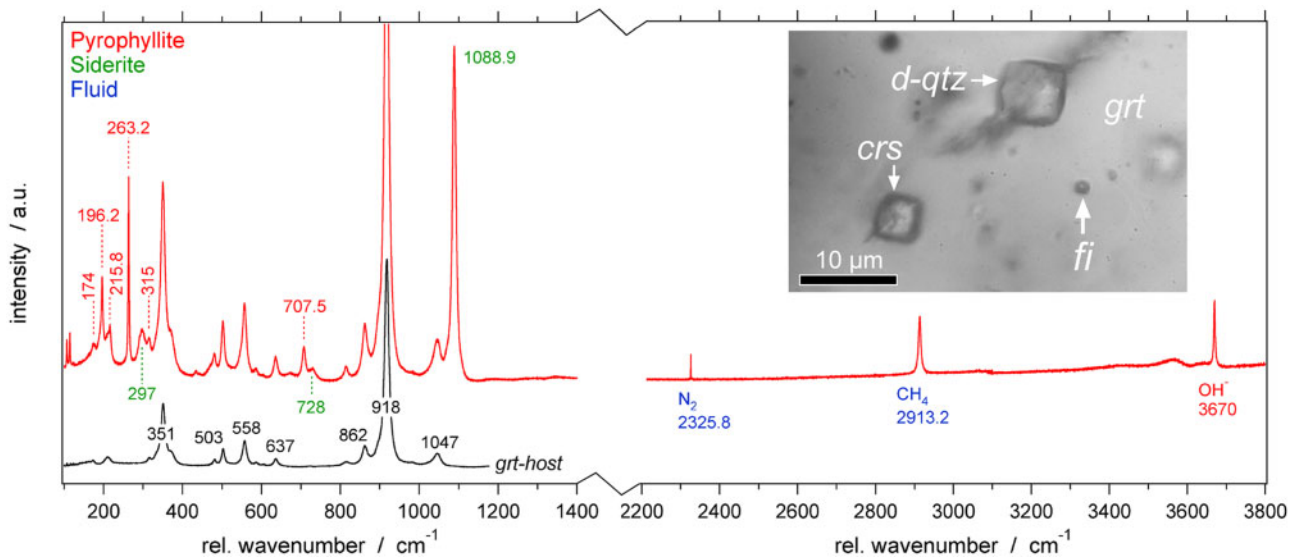

Fig. 12. Raman spectrum of a fluid inclusion in garnet compared to the signal of its host. A CH_4–N_2-rich fluid is identified in addition to small crystals of pyrophyllite and siderite. The photomicrograph illustrates the measured object (*fi*) that occurs in a cluster of a deformed quartz inclusion (*d-qtz*) and a cristobalite inclusion (*crs*) in garnet.

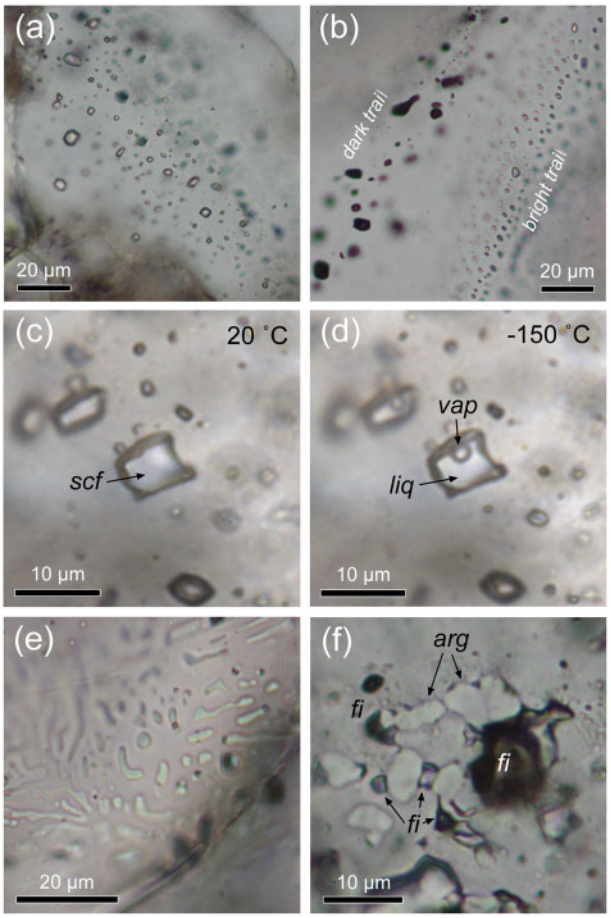

Fig. 13. Photomicrographs of solids and fluids in quartz nodules: (a) mono-phase CH_4-rich fluid inclusions; (b) trails of fluid inclusions with distinct concentrations of graphite, dark trail = high graphite concentration, bright trail = low graphite concentration; (c) and (d) example of phase separation in a CH_4-rich fluid inclusion at low temperature, a supercritical CH_4 phase (*scf*) is present at room temperature (20 °C), CH_4-rich liquid and vapour phase occur at low temperatures (*liq* and *vap*, respectively, -150 °C); (e) trail of aragonite inclusions, yellow-greenish worm-like crystals in quartz; (f) CH_4-rich fluid inclusions attached to aragonite.

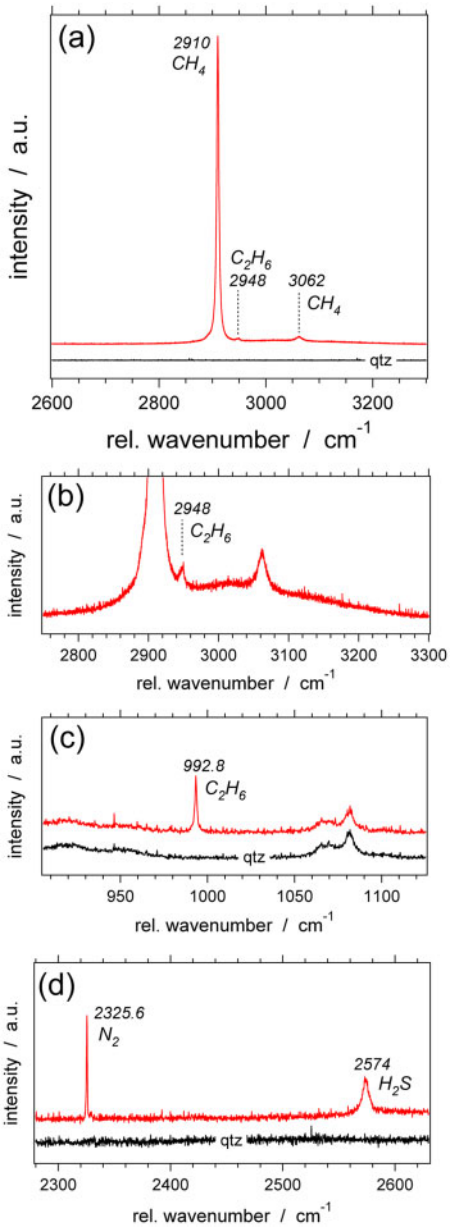

Fig. 14. Raman spectra of fluid components in fluid inclusions in quartz: (a) liquid-like CH_4, with a minor ethane band at 2948 cm^{-1}; (b) detail of (a) illustrating the ethane band; (c) narrow ethane band at 992·8 cm^{-1}; (d) narrow nitrogen band at 2325·6 cm^{-1} and hydrogen sulfide at 2574 cm^{-1}. Spectra of the quartz host (background signal) are illustrated for comparison.

The inclusions occur mainly in trails that are restricted within single quartz grains (Fig. 13a and b). Some inclusions with similar properties occur in clusters. The fluid inclusions have a regular and equant shape (see shape definition Bakker & Diamond, 2006), with diameters varying between 1 and 10 µm (Fig. 13c and d). A large part of these fluid inclusions contain graphite in addition to CH_4. This graphite is deposited on fluid inclusion walls, causing a dark appearance of the entire inclusion (Fig. 13b). Rapidly moving objects of sizes less than 1 µm in numerous dark fluid inclusions are identified as small flakes of graphite (presumable daughter crystals). Trails with clear graphite-free CH_4-rich fluid inclusions may occur adjacent to trails with dark graphite-rich fluid inclusions (Fig. 13b). Fluid inclusion trails are locally accompanied by aragonite inclusions (Fig. 13e and f), simultaneously trapped with a CH_4-rich fluid within the same cracks. Methane-rich inclusions are locally attached to these aragonite crystals within single trails. Solid inclusions in quartz consist of small euhedral garnet crystals (up to 20 µm in diameter), rutile needles (< 1 µm thickness, 5–10 µm length), graphite (equant shape, polycrystalline aggregates) and zircon.

Individual quartz crystals within clusters in the centre of garnets (Figs 6c and 11b) do not contain any fluid and solid inclusions. However, small fluid inclusions are detected by careful optical analyses at the contact between these quartz crystals and the garnet (Fig. 15). Many of these quartz crystals are coated with numerous tiny fluid inclusions (maximum diameter 0·5 µm). The

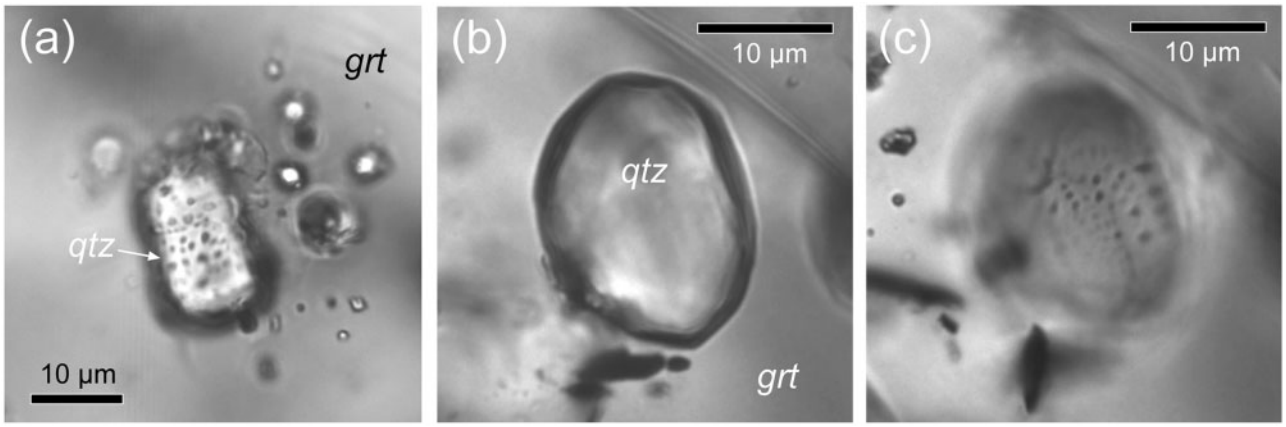

Fig. 15. Photomicrographs of tiny CH_4-rich fluid inclusions (< 0·5 μm) at the quartz surface, included within garnet (a). Images (b) and (c) represent different focus levels of the same quartz inclusion in garnet, to illustrates that fluid inclusions are not included in quartz, but are positioned at the contact quartz–garnet.

presence of CH_4 was detected with Raman spectroscopy in all of these inclusions.

Microthermometry

Microthermometry was used to measure homogenization temperatures of CH_4-rich fluid inclusions in quartz nodules. Three fluid inclusion assemblages are measured, and all inclusions homogenize into the liquid CH_4 phase at mode values varying between -119 °C and -128 °C (Fig.13c and d, Fig. 16, Supplementary Data Electronic Appendix 5). The histograms of all assemblages reveal approximately a normal distribution, and the variation in each assemblage is relatively small. The low concentrations of C_2H_6, N_2 and H_2S are assumed to have a negligible effect on treating the fluid as a pure CH_4 system. The calculated densities of the mode values are 0·349 to 0·367 g·cm^{-3}, corresponding to a molar volume of 43·7 to 45·9 cm^3·mol^{-1}.

Fluid inclusions that contain graphite reveal a methane Raman peak position at higher relative wavenumbers (2912 cm^{-1}) than inclusions without graphite (2910·4 cm^{-1}) (Fig. 17). This significant shift corresponds to lower CH_4 densities in graphite-bearing inclusions (c.f. Lin *et al.*, 2007; Zhang *et al.*, 2016). It must be noted that the so-called CH_4 densimeter according to Lin *et al.* (2007) and Zhang *et al.* (2016) cannot be used to calculate exact densities from Raman band positions, due to erroneous resolution considerations. A lower density of CH_4 is obtained by the consumption of CH_4 to produce graphite within fluid inclusions. This reaction also produces H_2, which may be completely lost by diffusion processes at granulitic metamorphic conditions.

Graphite crystallinity

Petrographical evidence and Raman spectroscopic analyses reveal the presence of three types of graphite in the garnetites (Fig. 18). Elongated graphite flakes occur within the garnet–cordierite–quartz matrix, with lengths up to 50 μm. These flakes occur as deformed (kinked) euhedral crystals within the granoblastic texture, and are not completely included in garnet, cordierite, and quartz. The Raman spectra of the flakes reveal a narrow G band (1581·1 cm^{-1}, Fig. 18a), in the absence of any D bands. Small equant crystals of graphite may occur in garnet, with a diameter of maximally 2 μm (Fig. 18b). These crystals reveal a similar Raman spectrum, with a clearly defined G band (1580·6 cm^{-1}) in the absence of D bands. The third type of graphite occurs in fluid inclusions (Fig. 18c). This graphite is present as a dispersed phase at fluid inclusion walls, and are rarely identified as tiny entrapped single crystals. Corresponding Raman spectra reveal a relatively low temperature pattern with a complex assemblage of G (1602·7 cm^{-1}) and D bands (main band at 1331·4 cm^{-1}).

The software IFORS (Lünsdorf *et al.*, 2014, 2017; Lünsdorf & Lünsdorf, 2016) is used to calculate formation conditions of the graphite (Supplementary Data Electronic Appendix 6). The first two types of graphite with the well-defined G band correspond to temperatures that exceed 600 °C, i.e. the maximum calibrated standard of the analytical procedure. The crystallisation temperatures of graphite in fluid inclusions are calculated at 300–310 ± 27 °C.

DISCUSSION

Cordierite–garnet geothermobarometry

Equilibrium thermodynamic modelling of the distribution of cations (Fe, Mg, Ca, Mn) between garnet and cordierite can be used to estimate high-grade metamorphic conditions. The first geothermometers included only the distribution of Fe and Mg (e.g. Hensen, 1977). Perchuk & Lavrent'eva (1983) added Mn to develop a geothermometer in the cordierite–garnet–biotite paragenesis. Bhattacharya *et al.* (1988), and Dwivedi *et al.* (1998) extended the geothermometer by including multicomponent Ca–Mg–Fe–Mn garnet compositions using thermodynamics of exchange reactions independently of the mineral paragenesis of the rock.

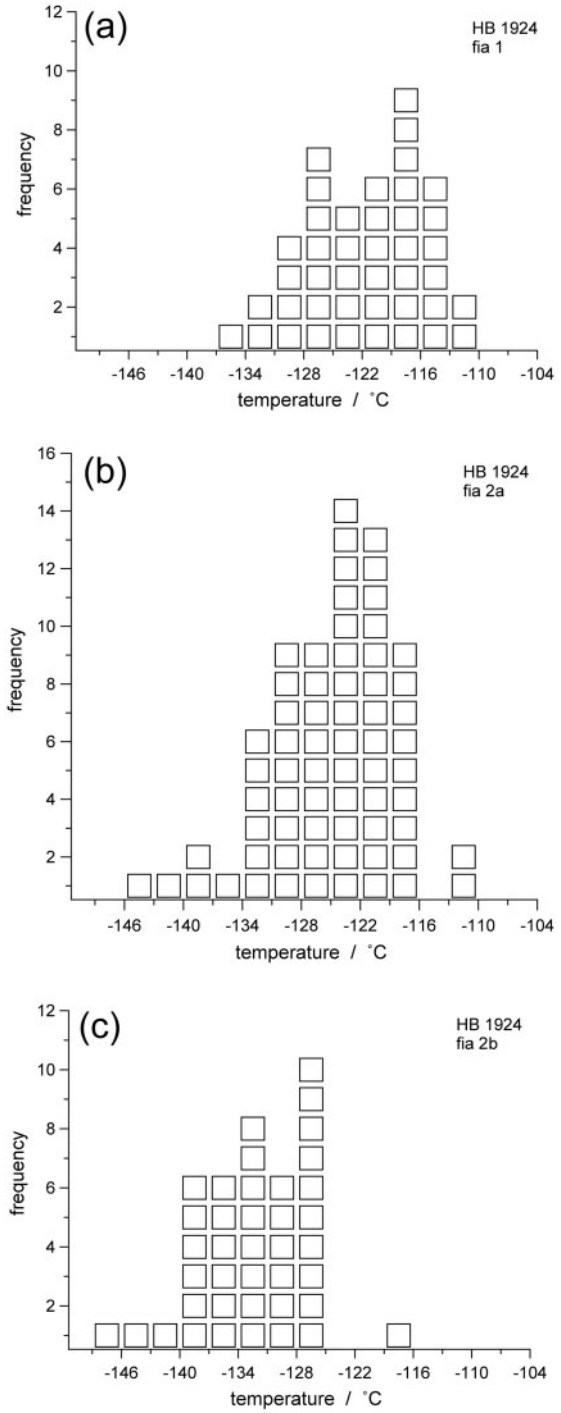

Fig. 16. Histograms of CH_4 homogenization temperatures in three fluid inclusion assemblages in quartz nodules.

Thermodynamic modelling of the cordierite–garnet–biotite assemblage was further improved by Kaneko & Miyano (2004) who included the effect of constant concentrations of Fe^{3+} in cordierite and garnet. A garnet–cordierite geothermobarometer including only the distribution of Fe and Mg was developed by Aranovich & Podlesskii (1983) in the cordierite–garnet–sillimanite–quartz paragenesis, similar to the paragenesis described in our study. Isopleths of the Mg-fraction in

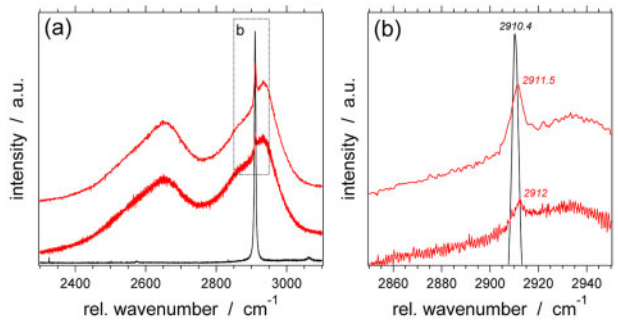

Fig. 17. Raman spectra of CH_4 in fluid inclusions without (2910·4 cm^{-1}) and with graphite (2911·5 and 2912 cm^{-1}).

cordierite and garnet have significantly different dP/dT slopes (see Fig. 10 in Aranovich & Podlesskii, 1983), consequently, the Fe/Mg distribution can be used to estimate metamorphic temperatures and pressures. A similar approach was presented by Lepezin & Korolyuk (1984) with isopleths for varying Mg-numbers of coexisting garnet and cordierite in the systems SiO_2–Al_2O_3–FeO–MnO–H_2O and SiO_2–Al_2O_3–FeO–MgO–H_2O.

The cordierite and garnet analyses from the garnetite sample Hb1933 (Supplementary Data Electronic Appendices 1 and 3) are used to estimate formation temperature and pressure conditions with the garnet–cordierite geothermobarometer by Aranovich & Podlesskii (1983). The conditions are calculated according to the relatively small variation in garnet and cordierite composition, in between limits illustrated in Fig. 19 and Table 6. Garnet composition is divided into two groups according to the distribution pattern of Fe and Mg mole fractions in dodecahedral sites. Most individual garnet grains are homogeneous without any trace of diffusion processes. The variability of temperature–pressure estimations is directly correlated with the range of observed compositional variation of garnets. This relatively small variation may be the result of compositional re-equilibration processes at high-grade metamorphic conditions. Calculated formation temperatures vary between 680–830 °C at pressures between 685–845 MPa (Fig. 20). The uncertainty in these numbers according to experimentally estimated values by Aranovich & Podlesskii (1983) is illustrated with the greenish-shaded area in Fig. 20 (i.e. ± 100 MPa and ± 15 °C). The grossular and spessartine fraction in the garnets is approximately 10% and does not significantly affect the calculations.

For comparison, the garnet–cordierite geothermometers by Perchuk & Lavrent'eva (1983), Bhattacharya *et al.* (1988) and Kaneko & Miyano (2004) are illustrated in Fig. 20. Temperatures calculated with the model of Perchuk & Lavrent'eva (1983) are relatively low at approximately 560–680 °C at 750 MPa, which is located in the kyanite stability field. However, sillimanite was identified in most rock samples, therefore, these temperatures are inconsistent with the mineralogy of the garnetites. Bhattacharya *et al.* (1988) included the grossular and spessartine fraction of garnets in

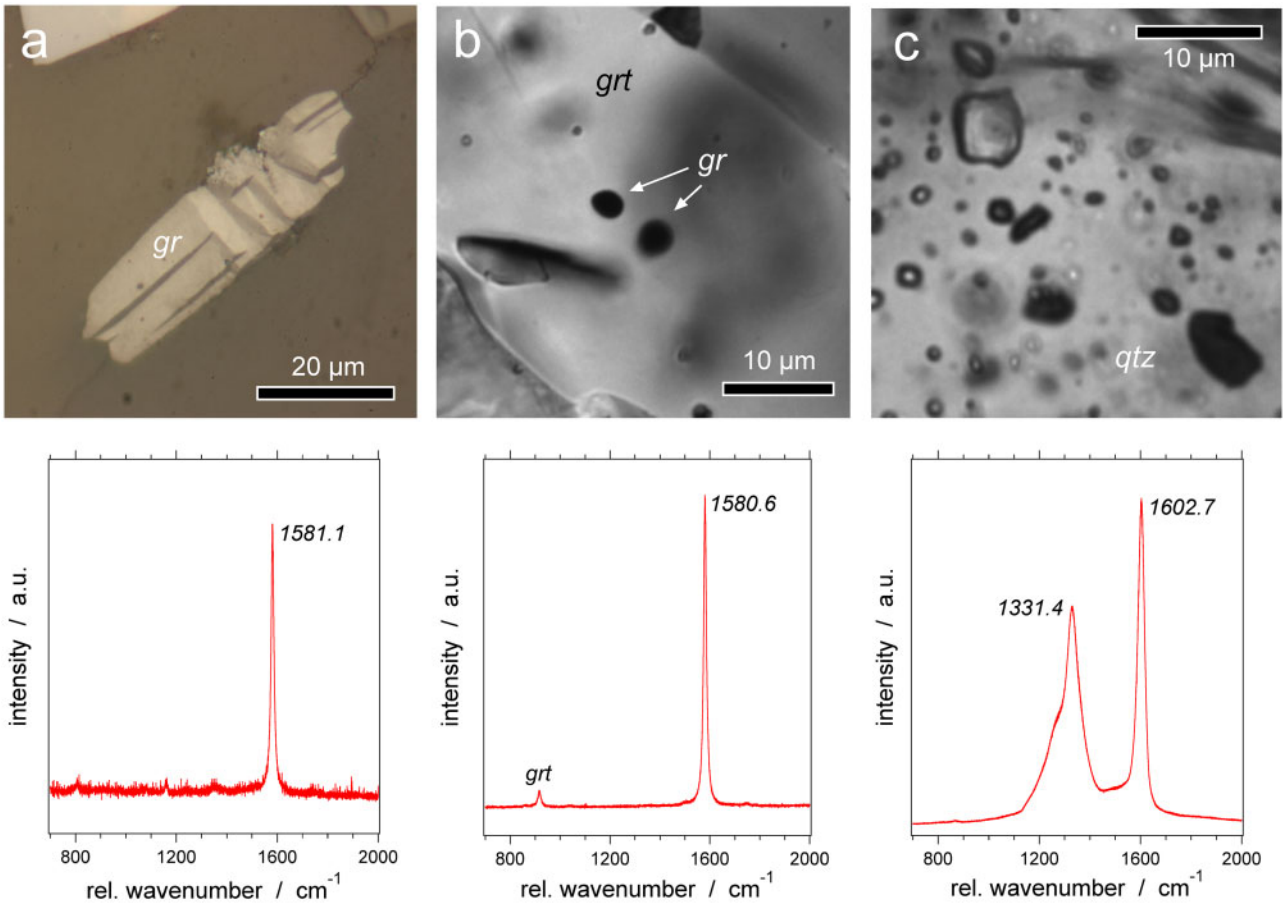

Fig. 18. Raman spectra of three types of graphite: (a) large graphite flakes in the matrix in reflective light microscopy, the Raman spectrum is obtained at about 20 μm below the surface to eliminate polishing artefacts; (b) small equant graphite crystals in garnet; (c) graphite in fluid inclusions, the opacity is related to the concentration of graphite.

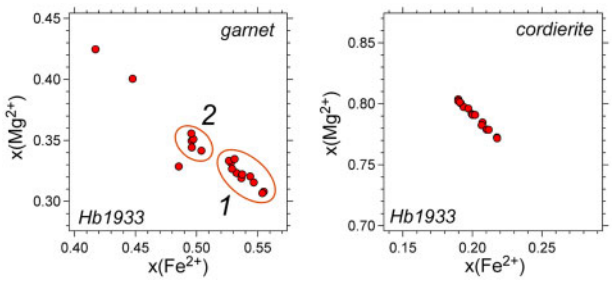

Fig. 19. Mole fractions Fe^{2+} versus Mg^{2+} in dodecahedral sites in garnet, and mole fractions Fe^{2+} versus Mg^{2+} in octahedral site in cordierite of sample Hb1933. Two compositional groups are identified in garnet (1) Fe# 0·53–0·55 and (2) Fe# around 0·50. The extreme values at Fe# = 0·45 and 0·42 are not taken into account.

thermodynamic modelling of the garnet–cordierite geothermometer, and their model results in calculated temperatures between 750–850 °C at 750 MPa. These temperatures are slightly higher than the model of Aranovich & Podlesskii (1983), but most of the values are within the uncertainty halo illustrated in Fig. 20. Kaneko & Miyano (2004) concluded that the presence of Fe^{3+} lowers the estimated temperatures of previously reported thermometers. The Fe^{3+} content in octahedral sites (*Y*) of our garnets is expressed in the andradite and skiagite fractions (Supplementary Data Electronic Appendix 1), and does not exceed 4 mole %. The calculated Fe^{3+} fraction is maximally 15 mole % of the total Fe. Fig. 20 illustrates that the geothermometer of Kaneko & Miyano (2004) is consistent with the lower temperature values of the model of Bhattacharya *et al.* (1988) and consistent with the average temperature estimates at 750 MPa from the model of Aranovich & Podlesskii (1983).

The composition of the fluid phase has a major impact on the pressure calculations, because it affects the activity of cordierite. The calculated *P–T* conditions in Fig. 20 correspond to values in the presence of a H_2O-rich fluid. Aranovich & Podlesskii (1983) argued that the modelled pressure difference between a dry (fluid-absent) and a wet system (i.e. water pressure is equal to total lithostatic pressure) is about 300 MPa. A high CO_2 content in the fluid phase would also diminish pressure estimations with about 160 MPa compared to a pure H_2O fluid. According to the observed fluid components in cordierite (Tables 4 and 5) it is expected that the fluid phase was highly enriched in CO_2 at peak metamorphic conditions.

Granulites form at temperatures above those for the closure of most thermometers and barometers (e.g.

Frost & Chacko, 1989), resulting in resetting processes during their exhumation. Relict textural features of minerals involved may evidence the reset, such as exsolution patterns and systematic zonations (diffusion patterns). Garnets with Mg-number around 0·34–0·36 (group 2 in Table 6, Figs 19 and 20) may represent the best-preserved original formation condition of the garnetites, at temperatures of 740–830 °C and pressures of 770–845 MPa.

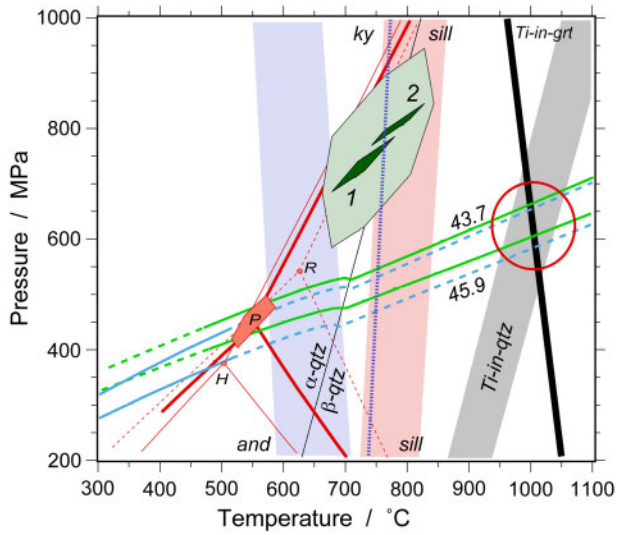

Fig. 20. Temperature–pressure phase diagram with isochores for the fluid inclusion assemblages in quartz nodules in garnetite. The green isochors for CH_4 of 43·7 and 45·9 cm^3/mol are calculated with Belonoshko & Saxena (1991) and can only be applied in high pressure–temperature ranges. The blue isochors represent the same values calculated with Setzmann & Wagner (1991), and can only be applied to temperatures up to 350 °C and 1000 MPa. The dashed green and blue lines are extrapolated isochores. The stability fields of Al_2SiO_5 polymorphs are illustrated with red-lines; H, Holdaway & Mukhopadhyay (1993); R, Richardson *et al.* (1969); P, Pattison (1992). The green area represents temperature–pressure conditions calculated with the garnet–cordierite–sillimanite–quartz geothermobarometer (Aranovich & Podlesskii, 1983). The numbers 1 and 2 correspond to the compositional variation of garnets (Fig. 19). The nearly vertical shaded areas are calculated with the geothermometers according to Perchuk & Lavrent'eva (1983, violet) and Bhattacharya *et al.* (1988, pink). The nearly vertical dark blue dotted line is the geothermometer according to Kaneko & Miyano (2004). The grey area and the thick black line are the Ti-in-qtz and the Ti-in-grt geothermometers according to Thomas *et al.* (2010) and Kawasaki & Motoyoshi (2016), respectively. The red circle at about 1000 °C and 650 MPa emphasizes the intersection of CH_4 isochores and Ti isopleths in quartz and garnet.

Geothermobarometry was also applied to gabbronorite in the EKC and garnet-bearing amphibolites of the upper metamorphic unit (Balykin *et al.*, 1991; Biryuzova & Pushkarev, 2007). Pyroxene thermometry according to Lindsley (1983) was applied to the gabbronorite revealing temperatures between 850–1000 °C. The *P–T* conditions of the garnet-bearing amphibolites were estimated at 650–750 °C (amphibole–garnet geothermometer according to Ravna, 2000), and at 500 – 700 MPa (plagioclase–amphibole geobarometer according to Molina *et al.*, 2015). These *P–T* estimates are consistent with values obtained from the garnet–cordierite geothermobarometer of garnetites in our study.

Ti geothermometry

Garnets reveal relatively high concentrations of Ti (Table 3, Supplementary Data Electronic Appendix 1). In addition, abundant Ti is also detected in quartz inclusions within garnet and in matrix quartz in nodules between garnet and cordierite grains (Fig. 8, Supplementary Data Electronic Appendix 2). The substitution of Ti in silicates that are formed at granulitic facies conditions can be used as geothermometers (e.g. Thomas *et al.*, 2010; Kawasaki & Motoyoshi, 2016). The occurrence of abundant rutile and ilmenite in garnetites may imply that the activity of TiO_2 in the system is close to 1. Subsequently, the empirical equation of Ti concentrations in quartz designed by Thomas *et al.* (2010) can be used to estimate temperature-pressure conditions from our TiO_2 analyses in quartz.

The high Ti solubility in quartz inclusions (0·031 ± 0·008 mass %) in single garnet grains (Figs 6c and 8a) corresponds to formation temperatures that are well above those calculated with the garnet–cordierite geothermobarometer, at temperatures between 1000–1080 °C at 800 MPa (Fig. 20). The variability of Ti concentrations in quartz nodules of 0·002–0·044 mass % (Figs 6a and 8b) may record re-equilibrated concentrations due to recrystallisation processes. Nachlas *et al.* (2014) demonstrated the mobility of Ti in quartz during specific deformation processes at high temperatures. Quartz grains that recrystallized via grain boundary processes equilibrated Ti contents that reflects *P–T* conditions of deformation. Quartz crystals that are entirely included in garnet may have been isolated and protected from subsequently deformation processes, and may, therefore, preserve original Ti content. Quartz within nodules between garnet and cordierite grains

Table 6: Range of calculated Fe^{2+}, $Mg^{2}+$, Mn^{2+} and Ca^{2+} composition of garnet and cordierite. Garnet group 1 and 2 are defined according to Fig. 19

	Mole fraction dodecahedral site X				Mole fraction octahedral site O	
	Garnet group 1		Garnet group 2		Cordierite	
Fe^{2+}	0·5539	0·5265	0·5039	0·4957	0·1898	0·2178
Mg^{2+}	0·3068	0·3333	0·3415	0·3556	0·8037	0·7717
Mn^{2+}	0·1030	0·1025	0·1182	0·1109	0·0065	0·0105
Ca^{2+}	0·0348	0·0377	0·0364	0·0377	–	–

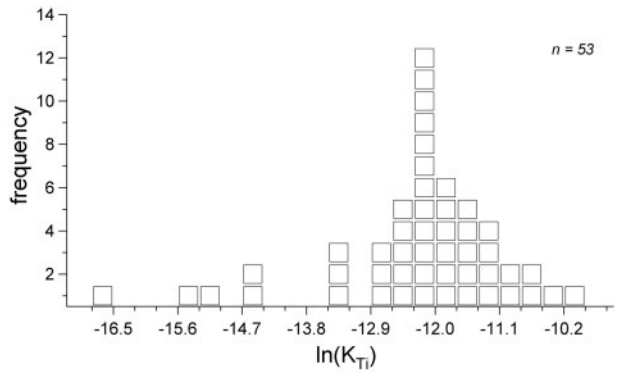

Fig. 21. Histogram of Ti concentrations in garnet from electron microprobe analyses, in terms of $\ln(K_{Ti})$ values (see Kawasaki & Motoyoshi, 2016).

may be exposed to deformation processes, and, therefore, may reequilibrate its Ti content to lower values. High Ti concentrations in quartz inclusions are relicts of a high-temperature metamorphic event that may have preceded the formation of the garnet–cordierite–sillimanite–quartz paragenesis, and that may be correlated with IBC-granulites (c.f. near-isobaric cooling *P–T* paths; Harley, 1989).

The solubility of TiO_2 in garnet increases with both temperature and pressure (e.g. Kawasaki & Motoyoshi, 2016) or with increasing Ca and Fe/Mg ratios (e.g. Ackerson *et al.*, 2017). The Ti solubility in garnet can be modelled with several substitution mechanisms. However, the use of Ti-in-garnet thermobarometry was considered infeasible due to the complexity of these substitution mechanisms (Ackerson *et al.* 2017). On the contrary, Kawasaki & Motoyoshi (2016) confirmed that the combined substitution $(Ti)^{octa}(Al)^{tetra} \Longleftrightarrow (Al)^{octa}(Si)^{tetra}$ is predominant and can be used as a geothermometer to estimate metamorphic conditions in the range 850–1300 °C, and 700– 2300 MPa. The variability of the Ti concentration in garnet (Supplementary Data Electronic Appendix 1) is illustrated in Fig. 21 with $ln(K_{Ti})$ values (as defined by Kawasaki & Motoyoshi, 2016). The average value $ln(K_{Ti}) = -12{\cdot}25$ correlates with most of the individual measurements (mode in Fig. 21), and corresponds to a temperature of about 1000 °C at 700 MPa (Fig. 20), similar to temperatures obtained with the Ti-solubility in quartz inclusions. The distribution of Ti-solubility reveals a smoothly declining tail towards higher values (up to -10·00, Fig. 21), which may reflect incomplete re-equilibration for specific garnet grains that were originally formed at higher temperature conditions. Sporadic lower values of $ln(K_{Ti})$ may reflect re-equilibration processes towards the conditions defined by garnet–cordierite geothermobarometry. Several aspects of the use of Ti-in-garnet thermometry require a critical evaluation of the method (e.g. Ackerson *et al.* 2017). The least squares fitting calculations of the equation designed by Kawasaki & Motoyoshi (2016) define standard errors that do not allow well-defined temperature estimations. For example, the average value $ln(K_{Ti}) = -12{\cdot}25$ results in a standard error of about 250 °C in temperature calculations at 700 MPa. Ti-diffusion in quartz and garnet at high-grade metamorphic conditions is another aspect that has to be considered for the interpretation of Ti concentrations (e.g. Carlson, 2006; Cherniak *et al.*, 2007; Spear *et al.*, 2012; Smit *et al.*, 2013). Compositional modifications of garnet and quartz during post-peak metamorphic conditions are facilitated by chemical cation diffusion. Compositional zoning in single crystals is a prerequisite to estimated peak temperatures with diffusion thermometers (e.g. Smit *et al.*, 2013). However, garnets from our study have nearly homogenous compositions without significant zoning. Compositional modifications brought about by diffusion processes at high temperatures must have affected entire grains due to relatively small grain sizes (0·5 mm in diameter).

Fluids in cordierite

Similar to fluid inclusion studies, the question may arise do cordierites contain a fluid that is trapped during crystal growth (so-called 'primary') in equilibrium with the chemistry of the rock, or are the conserved fluids the result of so-called post-entrapment modifications such as diffusion processes in a later stage of the geological history of a cordierite? Another important issue is the fractionation of fluid components between cordierite and pore fluid. Does the fluid composition in cordierite represent the fluid composition of the pore fluid?

H_2O and other volatiles in cordierite are mainly determined by infrared spectrographic methods (e.g. Goldman *et al.*, 1977) and by effusion methods (prolonged stepped heating) combined with a mass spectrometer (e.g. Harley & Carrington, 2001; Bul'bak & Shvedenkov, 2005). In theory, the intensity of the Raman bands of fluid species, i.e. the area of best-fit Gauss-Lorentz curves, can be used to calculate mass fractions within the cordierite structure (e.g. Kolesov & Geiger, 2000). This semi-quantitative technique was applied to CO_2 (Kaindl *et al.*, 2006; Haefecker *et al.*, 2013), but has not yet been developed for other fluid species such as H_2O, CH_4 and N_2. Various inconsistencies between the work of Kolesov & Geiger (2000), Kaindl *et al.* (2006) and Haefeker *et al.* (2013) in addition to internally incompatible equations in Haefeker *et al.* (2013) do not allow a definite calculation of the CO_2 mass fraction in cordierite with Raman spectroscopy. For example, a Mg-rich cordierite with a Fe-fraction, i.e. Fe/(Fe+Mg) less than 0·2 that reveal an intensity ratio (area) = 1 for the 923 cm^{-1} and 1382 cm^{-1} Raman bands contains 1·69 mass % CO_2 according to Haefeker *et al.* (2013) and 1·31 mass % CO_2 according to Kaindl *et al.* (2006). The relative difference of about 30% is much higher than the reported standard deviation of individual measurements.

In H_2O–CO_2 fluid mixtures, Johannes & Schreyer (1981) and Schreyer (1985) illustrated that CO_2 is strongly partitioned into the fluid phase, whereas cordierite

preferentially incorporates H_2O. Similar results were obtained for H_2O-CH_4 mixtures and H_2O-NH_3 mixtures (Bul'bak & Shvedenkov, 2005). According to these distribution patterns, the observed volatile composition of cordierites in garnetites from the metamorphic complex in the Khabarny Massif corresponds to a CO_2-rich fluid phase, in addition of minor amounts of N_2, H_2S and H_2O in the absence of CH_4. The contrast in fluid composition between fluid inclusions (CH_4-rich) and cordierite (CO_2–H_2O-rich) encourages a discussion about the ability of both environments to preserve its fluid content during the exhumation path of the rock, under varying temperature-pressure-redox conditions.

Modifications of volatile composition of cordierites

Preferential loss of H_2O known from re-equilibration experiments with fluid inclusions (e.g. Bakker & Jansen, 1990; Bakker, 2017) is also observed in experiments with cordierite. Aines & Rossman (1984) suggested that H_2O is degassing much faster than CO_2 from cordierites. For example, all H_2O was released at 800 °C, whereas 40 mole % of CO_2 remained in the channels. Heating to 900 °C was required to expel all CO_2. In addition, diffusional loss of H_2O at high temperatures and pressures is lowered by the presences of CO_2. Degassing at temperatures below 700 °C was extremely slow, and did not result in a significant loss of fluid components. Harley & Carrington (2001) reported an 'unrealistically' low H_2O content in cordierite compared to coexisting melt compositions due to post-equilibrium preferential H_2O loss. Isotope exchange diffusion experiments with H_2O–D_2O in cordierite (Bul'bak *et al.*, 1999) and in fluid inclusions (Doppler *et al.*, 2013; Bakker, 2017) have revealed that an original H_2O-rich fluid composition can be extremely enriched in D_2O at high temperatures in a D_2O-rich environment. Consequently, both fluids in channels in cordierite and in fluid inclusions may be seriously affected by post-entrapment modifications.

A compositional modification of volatiles in cordierite was also evidence by anhydrous experiments with volatile-free cordierite and pure CH_4 at 700 °C (Bul'bak *et al.*, 2002; Bul'bak & Shvedenkov, 2005). They detected H_2O within cordierite channels, and suggested the possibility of a reaction between CH_4 and cordierite framework oxygen. However, the channel structure of cordierite would be highly deformed with abundant vacancies, and this interaction is not charge-balanced.

Isochore construction

Is the entrapped CH_4-rich fluid in inclusions representative of peak metamorphic conditions of the garnetites? Comparison of the garnet–cordierite geothermometer with CH_4 densities reveals that the fluid properties do not correspond to peak metamorphic conditions (Fig. 20). Isochore construction of CH_4-rich fluid inclusions in quartz nodules results in a pressure calculation of 490–552 MPa at 800 °C according to Setzmann & Wagner (1991), and 518–569 MPa according to Belonoshko & Saxena (1991). These isochors are corrected for the volumetric properties of quartz at higher temperature and pressure. Garnet–cordierite geothermobarometric calculations reveal higher pressures (685–845 MPa) in the temperature range 680–830 °C. This difference may be obtained by post entrapment modifications of the CH_4-density to lower values, or by primary entrapment processes at a later stage of the exhumation history of the rock. However, the uncertainty in pressure estimates of garnet–cordierite geothermobarometry in the presence of a CO_2-rich fluid may reduce the misfit to fluid inclusion analyses.

CH_4 densities in fluid inclusions can be correlated with Ti geothermometry in quartz and garnet (red circle in Fig. 20). CH_4 isochores and Ti isopleths intersect at about 1000 °C and 650 MPa. Consequently, the CH_4-rich fluid may be directly related to a high-temperature metamorphic event that also resulted in the formation of cristobalite and high Ti concentration in quartz and garnet.

Fluids in the lower crust and mantle

At high-grade metamorphic conditions in the lower crust and mantle, it is assumed that a C–O–H fluid phase is completely buffered by solid rock, i.e. controlled by the chemistry and mineralogy of the rock (e.g. Saxena, 1988; Luth & Stachel, 2014). The composition of this fluid phase can be theoretically calculated according to the method of French (1966), Connolly (1995), Huizenga (2001) and Chu & Ague (2013), for example as applied to the metamorphic rock from Rogaland by Bakker & Jansen (1993). This buffering effect (i.e. internally controlled fluid composition) can be applied to a wide variety of environments, such as the lithosphere (both crust and upper mantle), asthenosphere, and mesosphere (deeper mantle). The calculations include a definition of the oxygen fugacity, which is representative for the rock in its original environment. Oxygen fugacity is a measure of oxidation in natural systems, and it can be calculated with and compared to specific mineral reactions, such as QFM (quartz–magnetite–fayalite) or IW (iron–wüstite) (e.g. Haas & Hemingway, 1992). The QFM oxygen fugacity represents a relatively oxidized environment in deep rock with H_2O–CO_2-rich fluids, whereas IW represents a relatively reduced environment with CH_4–H_2-rich fluids.

It is generally accepted that CH_4-rich fluids do not represent high-grade metamorphic conditions of granulites in the lower crust where the oxidation state is approximately QFM. The calculations illustrate that high temperature–pressure conditions are always associated with CO_2-rich fluids, and that a CH_4-rich fluid only occurs at low metamorphic conditions according to the selected oxygen buffer and the presence of graphite. Analyses of fluids in granulite-facies metamorphic rock have revealed that CO_2 is the dominant fluid species in addition to a saline aqueous fluid (e.g. Touret &

Dietvorst, 1983; Santosh *et al.*, 2004), and CH_4 is absent or a minor species. The origin of CH_4-rich and reduced fluids that was found in some fluid inclusion assemblages in granulites was suggested to be relatively low metamorphic conditions, in an early stage (prograde, e.g. Samson & William-Jones, 1991) or in a late stage (retrograde, e.g. Herms & Schenk, 1992) of the metamorphic *P*–*T* path. This assumption was confirmed by the relative low density of these CH_4-rich fluids.

These theoretical calculations do not exclude the possibility to have CH_4-rich fluids at deep crustal levels if the geological environment is highly reduced (e.g. Stachel *et al.*, 2017; Griffin *et al.*, 2018). The occurrence of high-density CH_4-rich fluid inclusions in granulite facies rock was reported in only few studies: Sila Massif, Calabria (Althaus & Istrate, 1990); and Rogaland, southwestern Norway (Kerkhof *et al.*, 1991). Kerkhof *et al.* (1991) described high density mixed CO_2–CH_4 fluid inclusions (up to 100 mole % CH_4) with traces of N_2 from quartz nodules in graphite-bearing garnet–cordierite leucogranitic rock, and high density mixed CO_2–CH_4–N_2 fluid inclusions (up to 92 mole % CH_4 and 91 mole % N_2) in a contact area between graphite-bearing garnetiferous and charnockitic migmatites. The latter contains also abundant high density aqueous inclusions. High density CH_4-rich and N_2-rich fluid inclusions in metapelites (mineral assemblage orthopyroxene, garnet, plagioclase, quartz) and basic granulites (mineral assemblage orthopyroxene, clinopyroxene, hornblende, garnet, plagioclase, quartz) were described by Althaus & Istrate (1990).

Touret (2009) and Frezzotti & Touret (2014) postulated that the dominant fluid phase in the shallow mantle (i.e. lithospheric mantle) at depths below 100 km is CO_2, locally associated with a brine. This type of fluid was assumed to be a 'deep external source' for granulitic fluids (c.f. mantle outgassing) in the lower crust. However, this environment is often characterized by low oxygen fugacities, close to IW (e.g. Green *et al.*, 1987; Rohrbach *et al.*, 2011, Griffin *et al.*, 2018). Green *et al.* (1987) suggest that the upper mantle below the asthenosphere contains remnants of primordial volatiles and minor carbon that have been modified to a reduced fluid dominated by CH_4, in addition to H_2O, H_2, and minor amounts of C_2H_6. The asthenosphere beneath oceanic crust itself is a fluid-absent region in which C–O–H volatiles are dissolved in melt fractions, separating CH_4-rich fluids in deep mantle (oxygen fugacity $\approx$ IW) from H_2O-rich and H_2O–CO_2 fluids in the lithosphere (oxygen fugacity $\approx$ QFM). Decompression of mafic to ultra-mafic melts in the asthenosphere that contain small amounts of carbon and a large hydroxyl content may exsolve a CH_4–H_2 rich fluid without redox interaction with the wall rocks (Green *et al.*, 1987; Foley, 2011). Abundant possible origins of a reduced C–O–H–N fluid system are discussed by Griffin *et al.* (2018), who investigated super-reducing conditions in lithospheric mantle xenoltihs in volcanic rock.

Garnetites in the metamorphic complex are associated with the EKC (mafic to ultramafic complex) that include abundant gabbronorite, websterite and dunite. These rocks may be the source of hot CH_4–H_2 rich fluids according to the previously mentioned theoretical considerations. During a decompressional phase in the tectonic history the released CH_4–H_2-rich fluid from mafic and ultra-mafic melt systems may have migrated into the adjacent upper unit of the metamorphic complex, and may have been trapped along healed cracks within quartz nodules in garnetites. Consequently, the CH_4-rich fluids have lower densities than expected from the metamorphic conditions according to garnet–cordierite geothermobarometry (Fig. 20). Hydrogen was not detected within fluid inclusions, but the presence of precipitated graphite is an indirect trace of diffusional loss of H_2. In theory, a graphite-unsaturated CH_4-H_2 rich fluid becomes oversaturated by preferential loss of H_2 or H_2O (e.g. Bakker & Jansen, 1993). This post-entrapment process also results in lower densities of the remaining CH_4 (c.f. Fig. 17). During a late stage in the exhumation history, graphite must have precipitated from the remaining increasingly metastable fluid in inclusions around 300–310 °C (see Supplementary Data Electronic Appendix 6).

Mineralogical and geochemical anomalies

The 'Results' includes a number of enigmatic observations: (1) aragonite in fluid inclusion assemblages in quartz nodules (Fig. 13e and f); (2) cristobalite in quartz clusters within garnets (Fig. 12); (3) siderite and pyrophyllite bearing CH_4-rich fluid inclusions in garnet (Fig. 12); and (4) CH_4-rich fluid inclusions coating quartz grains totally included in garnet (Fig. 15).

Aragonite is a $CaCO_3$ polymorph that may form in blueschist facies metamorphic rock, i.e. at high pressures between 1 GPa at 400 °C and 2 GPa at 900 °C (e.g. Buchner & Grapes, 2011). Therefore, the occurrence and formation conditions of aragonite in trails with CH_4-rich fluid inclusions in garnetites is highly enigmatic (Fig. 13e and f). The garnetites from the upper unit of the metamorphic complex do not have other mineralogical and textural evidence of a high pressure metamorphism. Aragonite may precipitate from aqueous solutions at pressures below the aragonite stability limit (e.g. Newton *et al.*, 1969). This implies that a $CaCO_3$-oversaturated fluid mixture of CH_4 and H_2O must have been present at formation condition of fluid inclusion assemblages in quartz nodules. The absence of H_2O in the present fluid inclusion assemblages may be caused by post-entrapment modifications such as preferential H_2O-leakage (e.g. Bakker & Jansen, 1990; Bakker, 2017). The transition of aragonite to calcite at 700 °C occurs at about 1650 MPa (e.g. thermodynamic modelling according to Holland & Powell, 2011). A hypothetical coexisting CH_4-rich fluid phase would have a density of 0·5462 g·cm^{-3} (Belonoshko & Saxena, 1991). This high density exceeds the triple point density of pure CH_4,

and does not correspond to the observed densities in associated fluid inclusions. It is unlikely that fluid inclusions with this dense fluid are able to survive subsequently a granulite facies metamorphism.

The SiO_2 inclusions in garnet from the garnetites are mainly mono-phase α-quartz crystals (Fig. 11), but locally cristobalite was indentified by Raman spectroscopy (Fig. 12, Supplementary Data Electronic Appendix 4). Cristobalite is a SiO_2 polymorph that is thermodynamically stable at very high temperatures (> 1470 °C) and relatively low pressures, which may occur naturally in volcanic rocks. Similar to aragonite, cristobalite may occur out of its field of stability. For example, cristobalite may develop at temperatures below 1000 °C from amorphous SiO_2 glass (e.g. Pagliari *et al.*, 2013), at 830 °C from quartz (Richet *et al.*, 1982), or at 1050 °C from β-quartz. Significant variations in transition temperatures may be caused by strain effects in individual grains (e.g. Leadbetter & Smith, 1976). The upper amphibolite-facies and granulite-facies conditions of the metamorphic complex in contact with the EKC are calculated at approximately 685–845 MPa and 680–830 °C, which is well below the limits of the cristobalite stability field. The occurrence of cristobalite is an argument for the preservation of exceptional high temperature conditions, in addition to the high Ti-concentration in quartz and garnet, and CH_4 density in fluid inclusions (Fig. 20). Cristobalite was identified in polycrystalline melt inclusions in garnets from high-pressure granulites by Ferrero *et al.* (2016) and Darling *et al.* (1997). Both Darling *et al.* (1997) and Ferrero *et al.* (2016) suggest a metastable crystallization process in high-pressure granulites resulting in cristobalite formation in melt inclusions. Ferrero *et al.* (2016) proposed a direct crystallization from a melt with a similar structure as cristobalite, and Darling *et al.* (1997) proposed an internal pressure decrease, caused by diffusive loss of H_2O. The deformation texture around some quartz and cristobalite inclusions (Fig. 11c and d) is similar to the observations of Ferrero *et al.* (2016), revealing decrepitation textures with sub-parallel cracks, or radial fractures in the garnet around the included quartz. These textures are also known from ultra-high pressure metamorphic gneisses with coesite inclusions in garnet (e.g. Parkinson, 2000; Song *et al.*, 2003). The origin of these textures is localized stress caused by the differential volumetric properties during an isothermal decompression (e.g. Korsakov *et al.*, 2007; Angel *et al.*, 2015).

Garnets in the garnetites include tiny CH_4-rich fluid inclusions (Fig. 12), with similar compositional properties as the fluid inclusion assemblages in quartz nodules. In addition, single quartz crystals within clusters in garnet are locally coated with similar numerous tiny CH_4-rich fluid inclusions (Fig. 15). This observation suggests that a reduced CH_4-rich fluid must have been present during the growth of garnet at peak metamorphic conditions. Densities of these inclusions could not be determined, due to optical limits. Siderite and pyrophyllite in fluid inclusions in garnet coexist with a highly reduced CH_4-rich fluid (Fig. 12), whereas these minerals do not occur in CH_4-rich fluid inclusion at the contact of quartz and garnet (Fig. 15). Siderite and pyrophyllite are common minerals trapped in fluid inclusions in granulitic garnets (e.g. Frost, 1979; Connolly, 1995; Carvalho *et al.*, 2018). The accompanying fluids were indentified as relatively oxidized: H_2O–CO_2 mixtures and dry CO_2-rich mixtures with minor amounts of CH_4 and N_2. Siderite and pyrophyllite are considered to be reaction products of the garnet-host and an original H_2O–CO_2-rich entrapped fluid (e.g. Carvalho *et al.*, 2018), i.e. so-called step-daughter crystals (e.g. Kleinefeld & Bakker, 2002). This reaction may have consumed the total amount of H_2O present within the inclusions. Therefore, both siderite and pyrophyllite in our samples may be the solid remnants of a earlier relatively oxidized system, which may also be evidenced by CO_2–H_2O-rich fluids absorbed in cordierite. A reduced hot CH_4–H_2-rich fluid must have subsequently flushed the rock-system, resulting in the formation of abundant CH_4-rich fluid inclusions before quartz crystal were entirely enclosed within growing garnet.

The analyses of fluids entrapped in fluid inclusions in quartz and garnet, and fluids in cordierite in garnetites reveal a strong contrast in composition, c.f. CH_4-rich versus CO_2–H_2O-rich, respectively. Both types of primary fluids may occur at high metamorphic conditions, but it is unlikely that both occur simultaneously in a mineral assemblage of a specific rock. The source of the CH_4-rich fluid is most probably an external mafic to ultramafic mantle rock system (IW buffered) that infiltrated a relatively oxidized lower crust system at granulite facies conditions (QFM buffered). The granulitic rocks were probably inundated with this reduce fluid, and the relatively minor amounts of H_2O–CO_2-rich fluids remained preserved only within cordierite, which preferentially absorbed the H_2O.

Comparison to the Salda metamorphic complex and the Ivrea–Verbano zone

Local geological settings and metamorphism in the EKC have been described in only few publications, mostly in Russian (Balykin *et al.*, 1991; Biryuzova & Pushkarev, 2007; Pushkarev *et al.*, 2007, 2008). Regional tectonic settings are defined by the arc–continent collision in the Uralides (e.g. Brown *et al.*, 2011). The negative εNdt of garnetites (Pushkarev *et al.*, 2008) illustrates that the granulites of the metamorphic complex have a continental crust signature, and can be regarded as a high-grade metamorphic sedimentary or igneous rock. The age of metamorphism is comparable with the age obtained for accompanying garnet amphibolite (415 ± 8 Ma; Pushkarev *et al.*, 2007). In addition to juxtaposed gabbronorite and similarity in *P–T* conditions with igneous rocks from the EKC, we suppose that the formation of granulite sequence in the metamorphic complex took place during magmatic underplating at the lower crustal level and further joint emplacement of

the entire sequence into upper crustal level as high-temperature plastic body (diapir) which was accompanied by plastic deformation and re-crystallization (blastomylonite shear zones). Magmatic underplating, i.e. intrusion of large masses of high temperature ultramafic to mafic mantle melts provides a strong positive thermal anomaly at the lower continental crustal level that is evidenced by the formation of two-pyroxene granulites and garnetites. In addition, high Ti concentrations in quartz and garnet, CH_4 densities in fluid inclusions, and the occurrence of cristobalite in garnetites may represent traces of an extreme high temperature metamorphism, up to 1000 °C, strengthening the idea of the development of a strong positive thermal anomaly. The variety of high-grade metamorphic sedimentary rocks in contact with EKC support the idea that it was a part of more ancient accretionary prism.

This model is similar to the kinzigite–granulite formation in the Ivrea–Verbano Zone in Italian Alps and other regions (Vielzeuf & Kornprobst, 1984; Zingg *et al.*, 1990; Henk *et al.*, 1997; Rivalenti *et al.*, 1997; Barboza *et al.*, 1999; Snoke *et al.*, 1999; Barboza & Bergantz, 2000). The Ivrea–Verbano zone is composed of a mafic complex (gabbroic, noritic and dioritic rocks) that intruded a granulite facies metamorphosed sedimentary sequence (e.g. Henk *et al.*, 1997; Carvalho *et al.*, 2018). Rivalenti *et al.* (1997) described garnetites between granulite-facies metapelites and mafic–ultramafic lithologies in the Ivrea–Verbano Zone, and discussed two processes that may have caused their petrogenesis. Sub-solidus diffusion (solid state) was excluded due to low mobility of elements, therefore, a melt fraction was considered to play a major role in the petrogenesis of garnetites: (1) anatexis with related metasomatism (dehydration melting); (2) garnetites segregation from a melt. Both processes can be evidenced by specific variations in garnet composition. Garnetites from the Ivrea–Verbano zone differ from our garnetites by rarely occurring cordierite (traces) and the absence of quartz. Rivalenti *et al.* (1997) did not analyse volatiles components and phases. Dehydration melting is mainly producing a H_2O-rich fluid phase, which is not detected in fluids of our garnetites.

True granulite of Paleozoic age, i.e. corresponding to *P–T* conditions of granulite facies, was distinguished in the Salda complex, that is situated in hinterland of the East-Uralian zone (Friberg *et al.*, 2000, 2002). It is represented by two-pyroxene gneiss, garnet–pyroxenites, pyroxene-bearing amphibolite and amphibolite of basic or intermediate composition. Most granulitic rocks of the Salda complex have island arc geochemical features, which demonstrate their subduction settings. Detailed isotopic studies, provided by Friberg *et al.* (2002), indicate the relatively young age of granulite and accompanied metamorphic and igneous rocks. The obtained data is varying from Ordovician to Carboniferous in age. The peak of granulite metamorphism took place at Devonian time, 380–360 Ma (Friberg *et al.*, 2002), and was proposed to be related with magmatic underplating processes in suprasubduction geological setting. The mineral assemblages in Salda granulites are equilibrated with the mineral paragenesis in surrounded gabbro and other magmatic rocks. The formation of granulites is related to the existence of a strong positive temperature anomaly that makes it different from the ultra-high pressure and low temperature Maksyutovo complex (see Fig. 1) of younger age. The origin of granulite facies metamorphic rock in the EKC is proposed to have occurred in similar geological settings as the Salda complex.

CONCLUSIONS

The metamorphic complex of the Khabarny Massif (Southern Urals) contains garnetites that are affected by granulite-facies metamorphic conditions. Geothermobarometric calculations with the cordierite–garnet assemblage reveal formation conditions of 680–830 °C and 685–845 MPa. The locally higher Mg content of garnets may refer to original peak metamorphic conditions up to 740– 830 °C and 770–845 MPa. Locally, SiO_2-inclusions in garnet provide evidence of a strong positive temperature anomaly by the preservation of cristobalite and the high titanium content of quartz.

Volatiles absorbed in cordierite consist mainly of H_2O, CO_2, N_2 and H_2S and represent a relative oxidized environment (QFM buffered) of granulite facies metamorphism. Fluid inclusions in quartz nodules contain mainly CH_4 with minor amounts of C_2H_6, N_2 and H_2S. Fluid inclusion assemblages are mainly defined in trails. These fluids are also trapped in primary inclusions at the contact between garnet and quartz crystals that are totally included in the core of garnets. Garnets themselves contain small fluid inclusions with a similar fluid. These fluids represent a relatively reduced environment (IW buffered) that must have overprinted the oxidized granulitic system. The origin of this fluid is most probably a deep mantle source that produces abundant CH_4–H_2 rich fluids upon cooling of an intrusive mafic–ultramafic magmatic complex in the lower crust, manifested by the East-Khabarny overturned stratified dunite–clinopyroxenite–websterite–gabbronorite complex in direct contact with the metamorphic complex. The density of the CH_4-rich fluids is consistent with the ultra-high temperature estimations of Ti geothermometry.

The presence of aragonite in CH_4-rich fluid inclusion assemblages in quartz nodules may represent metastable precipitation conditions well below its stability field. Graphite in fluid inclusions is precipitated at the inclusion walls around 300–320 °C, well below trapping conditions of a homogeneous CH_4-rich fluid.

Processes that formed the mineralogy and specific textures of garnetites in the metamorphic complex of the Khabarny Massif may have resulted from magmatic underplating of ultramafic to mafic mantle melts and further joint emplacement into upper crustal levels,

accompanied by plastic deformation and re-crystallization.

ACKNOWLEDGEMENT

Maik Zimmerman is greatly acknowledged for his help in the Eugen F. Stumpfl Microprobe Laboratory of the Montanuniversitaet Leoben, Austria. We thank Sankar Bose, V. Nandakumar and an anonymous reviewer for their constructive comments that help to improve and clarify the manuscript.

FUNDING

E. Pushkarev thanks to State scientific program (AAAA-A18-118052590029–6) for financial support.

SUPPLEMENTARY DATA

Supplementary data are available at *Journal of Petrology* online.

REFERENCES

Ackerson, M. R., Watson, E. B., Tailby, N. D. & Spear, F. S. (2017). Experimental investigation into the substitution mechanisms and solubility of Ti in garnet. *American Mineralogist* **102**, 158–172.

Aines, R. D. & Rossman, G. R. (1984). The high temperature behavior of water and carbon dioxide in cordierite and beryl. *American Mineralogist* **69**, 319–327.

Althaus, E. & Istrate, G. (1990). Granulite facies conditions derived from fluid inclusions: Sila Massif, Calabria, Italy. *Neues Jahrbuch für Mineralogie - Monatshefte* **2**, 65–75.

Angel, R. J., Nimis, P., Mazzucchelli, M. L., Alvaro, M. & Nestola, F. (2015). How large are departures from lithostatic pressure? Constraints from host-inclusion elasticity. *Journal of Metamorphic Geology* **33**, 801–813.

Aranovich, L. Y. & Podlesskii, K. K. (1983). The Cordierite-Garnet-Sillimanite-Quartz equilibrium: experiments and applications. In: Saxena, S. K. (ed.) *Kinetics and Equilibrium in Minerals Reactions*. Springer-Verlag, New-York, pp. 173–198.

Armbruster, T. (1985). Ar, N_2, and CO_2 in the structural cavities of cordierite, an optical and X-ray single-crystal study. *Physics and Chemistry of Minerals* **12**, 233–245.

Armbruster, T. & Bloss, F. D. (1982). Orientation and effects of channel H_2O and CO_2 in cordierite. *American Mineralogist* **67**, 284–291.

Bakker, R. J. (2003). Package FLUIDS 1. Computer programs for the analysis of fluid inclusion data and for modelling bulk fluid properties. *Chemical Geology* **194**, 3–23.

Bakker, R. J. (2016). Raman spectroscopy in fluid inclusion research. *In*: *Laser Meets Mineral - Raman Spectroscopy and Its Applications to Geosciences and Related Fields. Workshop SEG Student Chapter Leoben* 27–46.

Bakker, R. J. (2017). Re-equilibration processes in fluid inclusion assemblages. *Minerals* **7**, 117.

Bakker, R. J. & Diamond, L. W. (2006). Estimation of volume fractions of liquid and vapor phases in fluid inclusions, and definition of inclusions shape. *American Mineralogist* **91**, 635–657.

Bakker, R. J. & Jansen, J. B. H. (1990). Preferential water leakage from fluid inclusions by means of mobile dislocations. *Nature* **345**, 58–60.

Bakker, R. J. & Jansen, J. B. H. (1993). Calculated fluid evolution path versus fluid inclusion data in the COHN system as exemplified by metamorphic rocks from Rogaland, South-west Norway. *Journal of Metamorphic Geology* **11**, 357–370.

Balykin, P. A., Konnikov, E. G., Krivenko, A. P. & Lesnov, F. P. (1991). *Petrology of Post-Harzburgite Intrusions of the Kempirsay-Kabarny Ophiolite Association (Southern Urals).* In: Fershtater, G. B., Krivenko, A. P. (eds) Sverdlovsk. Ural Branch AS USSR. 160 p. (in Russian).

Barboza, S. A. & Bergantz, G. W. (2000). Metamorphism and anatexis in the mafic complex contact aureole, Ivrea zone, northern Italy. *Journal of Petrology* **41**, 1307–1327.

Barboza, S. A., Bergantz, G. W. & Brown, M. (1999). Regional granulite facies metamorphism in the Ivrea zone: Is the Mafic Complex the smoking gun or a red herring? *Geology* **27**, 447–450.

Belonoshko, A. & Saxena, S. K. (1991). A molecular dynamics study of the pressure-volume-temperature properties of super-critical fluids: II. CO_2, CH_4, CO, O_2, H_2. *Geochimica et Cosmochimica Acta* **55**, 3191–3208.

Belova, A. A., Ryazantsev, A. V., Razumovsky, A. A. & Degtyarev, K. E. (2010). Early Devonian Suprasubduction Ophiolites of the Southern Urals. *Geotectonics* **44**, 321–343.

Beyssac, O. & Lazzeri, M. (2012). Application of Raman spectroscopy to the study of graphitic carbons in the earth sciences. *European Mineralogical Union Notes in Mineralogy* **12**, 415–454.

Bhattacharya, A., Mazumdar, A. C. & Sen, S. K. (1988). Fe-Mg mixing cordierite: Constraints from natural data and implications for cordierite-garnet thermometry in granulites. *American Mineralogist* **73**, 338–344.

Biryuzova, A. P. & Pushkarev, E. V. (2007). High-Fe garnet paraamphibolites at the base of the Khabarny ophiolitic allochthon in the southern Urals. *Doklady Earth Sciences* **412**, 64–68.

Bohlen, S. R. (1991). On the formation of granulites. *Journal of Metamorphic Geology* **9**, 223–229.

Brown, D., Herrington, R. J. & Alvarez-Marron, J. (2011). Processes of arc-continent collision in the uralides. In: Brown, D. & Ryan, P. D. (eds) *Arc-Continent Collisions*. Springer-Verlag, Berlin Heidelberg, pp. 311–340.

Buchner, K. & Grapes, R. (2011). *Petrogenesis of Metamorphic Rocks*. Springer-Verlag, Berlin Heidelberg.

Bul'bak, T. A. & Shvedenkov, G. Y. (2005). Experimental study on incorporation of C-H-O-N fluid components in Mg-cordierite. *European Journal of Mineralogy* **17**, 829–838.

Bul'bak, T. A., Shvedenkov, G. Y. & Lepezin, G. G. (1999). Replacement of H_2O molecules by D_2O and CO_2 in the structural channels of cordierite. *Geokhimiya* **37**, 75–81.

Bul'bak, T. A., Shvedenkov, G. Y. & Lepezin, G. G. (2002). On saturation of magnesian cordierite with alkanes at high temperatures and pressures. *Physics and Chemistry of Minerals* **29**, 140–154.

Carlson, W. D. (2006). Rates of Fe, Mg, Mg, Mn, and Ca diffusion in garnet. *American Mineralogist* **91**, 1–11.

Carvalho, B. B., Bartoli, O., Ferri, F., Cesare, B., Ferrero, S., Remusat, L., Capizzi, L. S. & Poli, S. (2018). Anatexis and fluid regime of the deep continental crust: new clues from melt and fluid inclusions in metapelitic migmatites from Ivrea Zone (NW Italy). *Journal of Metamorphic Geology* **37**, 951–975.

Cherniak, D. J., Watson, E. B. & Wark, D. A. (2007). Ti diffusion in quartz. *Chemical Geology* **236**, 65–74.

Chu, X. & Ague, J. J. (2013). Phase equilibria for graphitic metapelite including solution of CO_2 in melt and cordierite: implications for dehydration, partial melting and graphite precipitation. *Journal of Metamorphic Geology* **31**, 843–862.

Connolly, J. A. D. (1995). Phase diagram methods for graphitic rocks and application to the system C-O-H-FeO-TiO_2-SiO_2. *Contributions to Mineralogy and Petrology* **119**, 94–116.

Darling, R. S., Chou, I.-M. & Bodnar, R. J. (1997). An occurrence of metastable cristobalite in high-pressure garnet granulite. *Science* **276**, 91–93.

Doppler, G., Bakker, R. J. & Baumgartner, M. (2013). Fluid inclusion modification by H_2O and D_2O diffusion: the influence of inclusion depth, size and shape in re-equilibration experiments. *Contributions to Mineralogy and Petrology* **165**, 1259–1274.

Dwivedi, S. B., Mohan, A. & Lal, R. K. (1998). Recalibration of the Fe-Mg exchange reaction between garnet and cordierite as a thermometer. *European Journal of Mineralogy* **10**, 281–289.

Ferrero, S., Ziemann, M. A., Angel, R. J., O'Brien, P. J. & Wunder, B. (2016). Kumdykolite, kokchetavite, and cristobalite crystallized in nanogranites from felsic granulites, Orlica?Snieznik Dome (Bohemian Massif): not evidence for ultrahigh?pressure conditions. *Contributions to Mineralogy and Petrology* **171**, doi 10.1007/s00410-015-1220-x.

Fershtater, G. B. & Bea F. (1996). Geochemical typification of ural ophiolites. *Geochemistry International* **34**, 171–193.

Fershtater, G. B., Montero, P., Borodina, N. S., Pushkarev, E. V., Smirnov, V. N. & Bea, F. (1997). Uralian magmatism: an overview. *Tectonophysics* **276**, 87–102.

Foley, S. F. (2011). A reappraisal of redox melting in the Earth's mantle as a function of tectonic setting and time. *Journal of Petrology* **52**, 1363–1391.

French, B. M. (1966). Some geological implications of equilibrium between graphite and a C-H-O gas phase at high temperatures and pressures. *Reviews of Geophysics* **4**, 223–253.

Frezzotti, M.-L. & Touret, J. L. R. (2014). CO_2, carbonate-rich melts, and brines in the mantle. *Geoscience Frontiers* **5**, 697–710.

Friberg, M., Juhlin, C., Beckholmen, M., Petrov, G. A. & Green, A. G. (2002). Palaeozoic tectonic evolution of the Urals in the light of the ESRU seismic experiments. *Journal of the Geological Society London* **159**, 295–306.

Friberg, M., Larionov, A., Petrov, G. A. & Gee, D. G. (2000). Paleozoic amphibolite-granulite facies magmatic complexes in the hinterland of the Uralide Orogen. *International Journal of Earth Sciences* **89**, 21–39.

Frost, B. R. (1979). Metamorphism of iron-formation: parageneses in the system Fe-Si-C-O-H. *Economic Geology* **74**, 775–785.

Frost, B. R. & Chacko, T. (1989). The granulite uncertainty principle: limitations on thermobarometry in granulites. *The Journal of Geology* **97**, 435–450.

Garrabos, Y., Chandrasekharan, V., Echargui, M. A. & Marsault-Herail, F. (1989). Density effect on the Raman fermi resonance in the fluid phases of CO_2. *Chemical Physics Letters* **160**, 250–256.

Goldman, D. S., Rossman, G. R. & Dollase, W. A. (1977). Channel constituents in cordierite. *American Mineralogist* **62**, 1144–1157.

Green, D. H., Falloon, T. J. & Taylor, W. R. (1987). Mantle-derived magmas - roles of variable source peridotite and variable C-H-O fluid composition. In: Mysen, B. O. (ed.) *Magmatic Processes: Physicochemical Principles*. The Geochemical Society, Special Publication **1**, University Park, Pennsylvania, pp. 139–154.

Griffin, W. L., Huang, J.-X., Thomassot, E., Gain, S. E. M., Toledo, V. & O'Reilly, S. Y. (2018). Super-reducing conditions in ancient and modern volcanic systems: sources and behaviour of carbon-rich fluids in the lithospheric mantle. *Mineralogy and Petrology* **112**, 101–114.

Haas, J. L. & Hemingway, B. S. (1992). Recommended standard electrochemical potentials and fugacities of oxygen for the solid buffers and thermodynamic data in the system iron-silicon-oxygen, nickel-oxygen, and copper-oxygen. *US Geological Survey, Open-File Report* 92–267.

Haefeker, U., Kaindl, R. & Tropper, P. (2013). Semi-quantitative determination of the Fe/Mg ratio in synthetic cordierite using Raman spectroscopy. *American Mineralogist* **97**, 1662–1669.

Harley, S. L. (1989). The origins of granulites: a metamorphic perspective. *Geological Magazine* **126**, 215–247.

Harley, S. L. & Carrington, D. P. (2001). The distribution of H_2O between cordierite and granitic melt: H_2O incorporation in cordierite and its application to high-grade metamorphism and crustal anatexis. *Journal of Petrology* **42**, 1595–1620.

Harley, S. L., Thompson, P., Hensen, B. J. & Buick, I. S. (2002). Cordierite as a sensor of fluid conditions in high-grade metamorphism and crustal anatexis. *Journal of Metamorphic Geology* **20**, 71–86.

Harlov, D. E. (2012). The potential role of fluids during regional granulite-facies dehydration in the lower crust. *Geoscience Frontiers* **3**, 813–827.

Henk, A., Franz, L., Teufel, S. & Oncken, O. (1997). Magmatic underplating, extension, and crustal reequilibration: insights from a cross-section through the Ivrea Zone and Strona-Cenert Zotte, Northern Italyl. *The Journal of Geology* **105**, 367–377.

Hensen, B. J. (1977). Cordierite-garnet bearing assemblages as geothermometers and barometers in granulite facies terranes. *Tectonophysics* **43**, 73–88.

Herms, P. & Schenk, V. (1992). Fluid inclusions in granulite-facies metapelites of the Hercynian ancient lower crust of the Serre, Calabria, Southern Italia. *Contributions to Mineralogy and Petrology* **112**, 393–404.

Holdaway, M. J. & Mukhopadhyay, B. (1993). A re-evaluation of the stability relations of andalusite: thermochemical data and phase diagram for the aluminium silicates. *American Mineralogist* **78**, 298–315.

Holland, T. J. B. & Powell, R. (2011). An improved and extended internally consistent thermodynamic dataset for phases of petrological interest, involving a new equation of state for solids. *Journal of Metamorphic Geology* **29**, 333–383.

Huizenga, J. M. (2001). Thermodynamic modelling of C-O-H fluids. *Lithos* **55**, 101–114.

Johannes, W. & Schreyer, W. (1981). Experimental introduction of CO_2 and H_2O in Mg-cordierite. *American Journal of Science* **281**, 299–317.

Kaindl, R., Tropper, P. & Deibl, I. (2006). A semi-quantitative technique for determination of CO_2 in cordierite by Raman spectroscopy in thin sections. *European Journal of Mineralogy* **18**, 331–335.

Kaneko, Y. & Miyano, T. (2004). Recalibration of mutually consistent garnet-biotite and garnet–cordierite geothermometers. *Lithos* **73**, 255–269.

Kawasaki, T. & Motoyoshi, Y. (2016). Ti-in-garnet thermometer for ultrahigh-temperature granulites. *Journal of Mineralogical and Petrological Sciences* **111**, 226–240.

Kerkhof, A. M., van den Kronz, A. & Simon, K. (2014). Deciphering fluid inclusions in high-grade rocks. *Geoscience Frontiers* **5**, 683–695.

Kerkhof, A. M., van den Touret, J. L. R., Maijer, C. & Jansen, J. B. H. (1991). Retrograde methane-dominated fluid

inclusions from high-temperature granulites of Rogaland, SW Norway. *Geochimica et Cosmochimica Acta* **55**, 2533–2544.

Kiseleva, D. V., Deryugina, L. K., Gorbunova, N. P. & Khiller, V. V. (2007). Inter-laboratory quality control analysis as a part of the GeoPT laboratory testing program. Year-Book-2006, Ekaterinburg, Institute of Geology and Geochemistry UB RAS, pp 302–305.

Kleinefeld, B. & Bakker, R. J. (2002). Fluid inclusions as microchemical systems: evidence and modelling of fluid host interactions in plagioclase. *Journal of Metamorphic Geology* **20**, 845–858.

Kolesov, B. A. & Geiger, C. A. (2000). Cordierite II: the role of CO_2 and H_2O. *American Mineralogist* **85**, 1265–1274.

Korsakov, A. V., Hutsebaut, D., Theunissen, K., Vandenabeele, P. & Stepanov, A. S. (2007). Raman mapping of coesite inclusions in garnet from the Kokchetav Massif (Northern Kazakhstan). *Spectrochimica Acta Part A: Molecular and Biomolecular Spectroscopy* **68**, 1046–1052.

Leadbetter, A. J. & Smith, T. W. (1976). The α-β transition in the cristobalite phase of SiO_2 and $AlPO_4$ II. Calorimetric studies. *The Philosophical Magazine* **33**, 113–119.

Lennykh, V. I., Pankov, Y. D. & Petrov, V. I. (1978). *Petrology and metamorphism of migmatite complex*. In: Petrology and iron-ore deposits of the Taratash complex. Sverdlovsk, Ural Scientific Center, Academy of Sciences of USSR. 3–45 (in Russian).

Lepezin, G. G. & Korolyuk, V. N. (1984). The dynamic of zonal garnet growth in bivariant assemblages. *Russian Geology and Geophysics* **12**, 116–126.

Lin, F., Bodnar, R. J. & Becker, S. P. (2007). Experimental determination of the Raman CH4 symmetric stretching (m1) band position from 1–650 bar and 0.3–22 °C: application to fluid inclusion studies. *Geochimica et Cosmochimica Acta* **71**, 3746–3756.

Lindsley, D. H. (1983). Pyroxene thermometry. *American Mineralogist* **68**, 477–493.

Locock, A. J. (2008). An Excel spreadsheet to recast analyses of garnet into end-member. *Computers & Geosciences* **34**, 1769–1780.

Lünsdorf, N. K. & Lünsdorf, J. O. (2016). Evaluating Raman spectra of carbonaceous matter by automated, iterative curve-fitting. *International Journal of Coal Geology* **160-161**, 51–62.

Lünsdorf, N. K., Dunkl, I., Schmidt, B. C., Rantitsch, G. & von Eynatten, H. (2014). Towards a higher comparability of geothermometric data obtained by Raman spectroscopy of carbonaceous material. Part 1: Evaluation of biasing factors. *Geostandards and Geoanalytical Research* **38**, 73–94.

Lünsdorf, N. K., Dunkl, I., Schmidt, B. C., Rantitsch, G. & von Eynatten, H. (2017). Towards a higher comparability of geothermometric data obtained by Raman spectroscopy of carbonaceous material. Part 2: A revised geothermometer. *Geostandards and Geoanalytical Research* **41**, 593–612.

Luth, R. W. & Stachel, T. (2014). The buffering capacity of lithospheric mantle: implications for diamond formation. *Contributions to Mineralogy and Petrology* **168**, 1083.

Molina, J. F., Moreno, J. A., Castro, A., Rodríguez, C. & Fershtater, G. B. (2015). Calcic amphibole thermobarometry in metamorphic and igneous rocks: New calibrations based on plagioclase/amphibole Al-Si partitioning and amphibole/-liquid Mg partitioning. *Lithos* **232**, 286–305.

Nachlas, W. O., Whitney, D. L., Teyssier, C., Bagley, B. & Mulch, A. (2014). Titanium concentrations in quartz as a record of multiple deformation mechanisms in an extensional shear zone. *Geochemistry, Geophysics, Geosystems* **15**, 1374–1397.

Newton, R. C., Goldsmith, J. R. & Smith, J. V. (1969). Aragonite crystallization from strained calcite at reduced pressures and its bearing on aragonite in low-grade metamorphism. *Contributions to Mineralogy and Petrology* **22**, 335–348.

Pagliari, L., Dapiaggi, M., Pavese, A. & Francescon, F. (2013). A kinetic study of the quartz-cristobalite phase transition. *Journal of the European Ceramic Society* **33**, 3403–3410.

Parkinson, C. D. (2000). Coesite inclusions and prograde compositional zonation of garnet in whiteschist of the HP-UHPM Kokchetav massif, Kazakhstan: a record of progressive UHP metamorphism. *Lithos* **52**, 215–233.

Pattison, D. R. M. (1992). Stability of andalusite and sillimanite and the Al_2SiO_5 triple point: constraints from the Ballachulish aureole, Scotland. *The Journal of Geology* **100**, 423–446.

Perchuk, L. L. & Lavrent'eva, I. V. (1983). Experimental Investigation of Exchange Equilibria in the System Cordierite-Garnet-Biotite. In: Saxena, S. K. (ed.) *Kinetics and equilibrium in minerals reactions*. Springer-Verlag, Berlin Heidelberg, pp. 199–239.

Puchkov, V. N. (2000). Paleogeodynamics of the Southern and Middle Urals. Dauria, Ufa, p 146. (in Russian).

Puchkov, V. N. (2002). Paleozoic Evolution of the East European Continental Margin Involved into the Urals // Mountain Building in the Uralides: Pangea to the Present. In: Brown, D., Juhlin, C., Puchkov, V. N. (eds) *AGU Geophysical Monograph Series* **132**, Wiley, pp. 9–32.

Puchkov, V. N. (2009). The evolution of the Uralian orogen. *Geological Society, London, Special Publications* **327**, 161–195.

Puchkov, V. N. (2013). Structural stages and evolution of the Urals. *Mineralogy and Petrology* **107**, 3–37.

Pushkarev, E. V., Biryuzova, A. P. & Serov, P. A. (2008). *Spinel-kyanite-cordierite garnetite – the indicators of peak conditions and age of granulite metamorphism in contact aureole of the East-Khabarny ultramafic complex in the Southern Urals*. Year-Book-2007. Institute of Geology and Geochemistry UB RAS. Ekaterinburg, 173–181 (In Russian).

Pushkarev, E. V., Serov, P. A. & Biryuzova, A. P. (2007). Isotope Sm-Nd data on the Late Silurian-Early Devonian age of dynamometamorphism at the base of ophiolitic allochthon in the Sakmara Zone of the southern Urals. *Doklady Earth Sciences* **413**, 198–202.

Ravna, E. K. (2000). Distribution of Fe^{2+} and Mg between coexisting garnet and hornblende in synthetic and natural systems: an empirical calibration of the garnet-hornblende Fe-Mg geothermometer. *Lithos* **53**, 265–277.

Richardson, W., Gilbert, M. C. & Bell, P. M. (1969). Experimental determination of kyanite-andalusite and andalusite-sillimanite equilibria: the aluminium silicate triple point. *American Journal of Science* **267**, 259–272.

Richet, P., Bottinga, Y., Denielou, L., Petitet, J. P. & Tequi, C. (1982). Thermodynamic properties of quartz, cristobalite and amorphous SiO_2: drop calometry measurements between 1000 and 1800 K and a review from 0 to 2000 K. *Geochimica et Cosmochimica Acta* **46**, 2639–2658.

Rigby, M. J. & Droop, G. T. R. (2008). The cordierite fluid monitor: case studies for and against its potential application. *European Journal of Mineralogy* **20**, 693–712.

Rivalenti, G., Mazzucchelli, M., Barbieri, M. A., Parent, M., Schmid, R. & Zanetti, A. (1997). Garnetite forming processes in the deep crust: the Val Fiorina case study (Ivrea–Verbano

zone, NW Alps). *European Journal of Mineralogy* **9**, 1053–1071.

Rohrbach, A., Ballhaus, C., Ulmer, P., Golla-Schindler, U. & Schönbohm, D. (2011). Experimental evidence for a reduced metal-saturated upper mantle. *Journal of Petrology* **52**, 717–731.

Ronkin, Y. L., Sindern, S., Maslov, A. V., Matukov, D. I., Kramm, U. & Lepikhina, O. P. (2007). Oldest (3.5 Ga) Zircons of the Urals: U–Pb (SHRIMP-II) and TDM constraints. *Doklady Earth Sciences* **415**, 860–865.

Samson, I. M. & William-Jones, A. E. (1991). C-O-H-N-salt fluids associated with contact metamorphism, McGerrigle Mountains, Quebec: a Raman sepctroscopic study. *Geochimica et Cosmochimica Acta* **55**, 169–177.

Santosh, M., Tsunogae, T. & Yoshikura, S.-I. (2004). Ultrahigh density" carbonic fluids in ultrahigh-temperature crustal metamorphism. *Journal of Mineralogical and Petrological Sciences* **99**, 164–179.

Savelieva, G. N. (2011). Ophiolites in European Variscides and Uralides: Geodynamic settings and metamorphism. *Geotectonics* **45**, 439–452.

Saxena, S. K. (1988). Oxidation state of the mantle. *Geochimica et Cosmochimica Acta* **53**, 89–95.

Schreyer, W. (1985). Experimental studies on cation substitutions and fluid incorporation in cordierite. *Bulletin de Minéralogie* **108**, 273–291.

Setzmann, U. & Wagner, W. (1991). A new equation of state and tables of thermodynamic properties for methane covering the range from the melting line to 625 K at pressures up to 1000 MPa. *Journal of Physical and Chemical Reference Data* **20**, 1061–1155.

Sindern, S., Hetzel, R., Schulte, B. A., Kramm, U., Ronkin, Y. L., Maslov, A. V. & Lepikhina, O. P. (2005). Proterozoic magmatic and tectonometamorphic evolution of the Taratash complex, Central Urals, Russia. *International Journal of Earth Sciences* **94**, 319–335.

Smit, M. A., Scherer, E. E. & Mezger, K. (2013). Peak metamorphic temperatures from cation diffusion zoning in garnet. *Journal of Metamorphic Geology* **31**, 339–358.

Snoke, A. W., Kalakay, T. J., Quick, J. E. & Sinigoi, S. (1999). Development of a deep-crustal shear zone in response to syntectonic intrusion of mafic magma into the lower crust, Ivrea–Verbano Zone, Italy. *Earth and Planetary Science Letters* **166**, 31–45.

Song, S. G., Yang, J. S., Xu, Z. Q., Liou, J. G. & Shi, R. D. (2003). Metamorphic evolution of the coesite-bearing ultrahigh--pressure terrane in the north Qaidam. *Journal of Metamorphic Geology* **21**, 631–644.

Spear, F. S., Ashley, K. T., Webb, L. E. & Thomas, J. B. (2012). Ti diffusion in quartz inclusions: implications for metamorphic time scales. *Contributions to Mineralogy and Petrology* **164**, 977–985.

Stachel, T., Chacko, T. & Luth, R. W. (2017). Carbon isotope fractionation during diamond growth in depleted peridotite: Counterintuitive insights from modelling water-maximum CHO fluids as multi-component systems. *Earth and Planetary Science Letters* **473**, 44–51.

Suggate, S. M. & Hall, R. (2018). Using Detrital Garnet Compositions to Determine Provenance: A New Compositional Database and Procedure (2014). In: Scott, R. A., Smyth, H. R., Morton, A. C. & Richardson, N. (eds) *Sediment Provenance Studies in Hydrocarbon Exploration and Production*. Geological Society, London, Special Publications **386**, 373–393.

Thomas, J. B., Watson, E. B., Spear, F. S., Shemella, P. T., Nayak, S. K. & Lanzirotti, A. (2010). TitaniQ under pressure: the effect of pressure and temperature on the solubility of Ti in quartz. *Contributions to Mineralogy and Petrology* **160**, 743–759.

Touret, J. L. R. (2001). Fluids in metamorphic rocks. *Lithos* **55**, 1–25.

Touret, J. L. R. (2009). Mantle to lower-crust fluid/melt transfer through granulite metamorphism. *Russian Geology and Geophysics* **50**, 1052–1062.

Touret, J. L. R. & Dietvorst, P. (1983). Fluid inclusions in high-grade anatectic metamorphites. *Journal of the Geological Society* **140**, 635–649.

Varlakov, A. S. (1978). *Petrography, Petrochemistry and Geochemistry of Ultramafites of the Orenburg Part of the Urals*. Nauka, Moscow (in Russian).

Vielzeuf, D. & Kornprobst, J. (1984). Crustal splitting and the emplacement of Pyrenean lherzolites and granulites. *Earth and Planetary Science Letters* **67**, 87–96.

Votyakov, S. L., Kiseleva, D. V., Shagalov, S. E., Cherednichenko, N. V., Deryugina, L. K., Denisov, S. A., Chempalov, A. P., Uzkikh, S. E. & Orekhov, A. A. (2006). Multi-element analysis of geological samples by inductively coupled plasma mass spectrometry on an ELAN 9000. Year-Book-2005, Ekaterinburg, Institute of Geology and Geochemistry UB RAS, pp 425–430.

Windley, B. F. (1981). Phanerozoic granulites. *Journal of the Geological Society* **138**, 745–751.

Zhang, J., Qiao, S., Lu, W., Hu, Q., Chen, S. & Liu, Y. (2016). An equation for determining methane densities in fluid inclusions with Raman shifts. *Journal of Geochemical Exploration* **171**, 20–28.

Zingg, A., Handy, M. R., Hunziker, J. C. & Schmid, S. M. (1990). Tectonometamorphic history of the Ivrea Zone and its relationship to the crustal evolution of the Southern Alps. *Tectonophysics* **182**, 169–192.